J. Fluid Mech. (2022), *vol*. 947, A14, doi:10.1017/jfm.2022.619

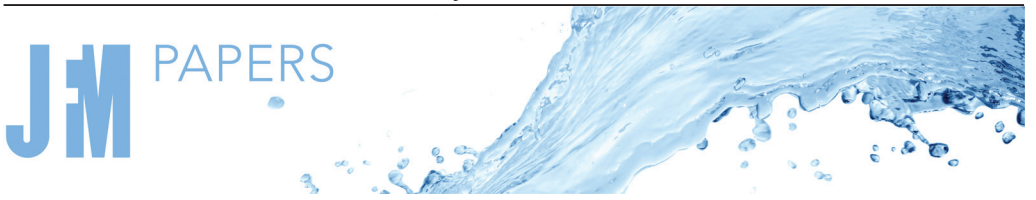

Shock-induced leading-edge separation in hypersonic flows

L. Srinath[1],‡, R. Sriram[2], P. Akhilesh[1] and G. Jagadeesh[1],†

[1]Laboratory for Hypersonic and Shockwave Research, Department of Aerospace Engineering, Indian Institute of Science, Bengaluru 560012, India

[2]Department of Aerospace Engineering, Indian Institute of Technology, Madras 560012, India

(Received 27 May 2021; revised 3 July 2022; accepted 9 July 2022)

We investigate the leading-edge separation, also called negligible boundary-layer thickness separation, induced by an impinging shock on a sharp flat plate. The canonical impinging shock wave/boundary-layer interaction configuration consisting of a wedge and a plate wall, placed in hypersonic free stream, is used for the investigations. We first construct a theoretical model for the leading-edge separated flow field (LESF) which predicts separation bubble geometry and surface pressure distribution as a function of three parameters: free-stream Mach number, wedge angle and the reattached flow turning angle. Markedly different predictions of the separated flow field are obtained for an oblique and a near normal reattachment on the plate surface. Experiments in a shock tunnel at a nominal Mach 6 flow, with an impinging shock generated by a wedge of angle 26.6°, are used to validate the model. Schlieren flow visualization using a high-speed camera and surface pressure measurements using fast response piezoelectric sensors are the diagnostics employed. For a range of shock impingement locations, the LESFs are observed to be geometrically similar and in good agreement with the LESF model. When the impingement location gets closer to the leading edge, it is observed from experiments that the flow field is no longer geometrically similar, and the separation angle increases as the impingement gets closer to the leading edge beyond the range of similarity. The work thereby offers an elaborate description of the leading-edge separated flow when shock impingement occurs near the plate leading edge.

Key words: hypersonic flow, gas dynamics, boundary layer separation

† Email address for correspondence: jaggie@aero.iisc.ernet.in
‡ Present address: Physics of Fluids, Faculty of Science and Technology, University of Twente, Enschede 7500AE, Netherlands.

1. Introduction

The interaction between a shock wave and a boundary layer, termed shock wave/boundary-layer interaction (SWBLI), is commonly encountered in high-speed flows. Examples include: a stationary shock wave interacting with the nozzle boundary layer in the over-expanded operation of a rocket nozzle; a ramp shock impinging on a cowl plate boundary layer in the operation of a scramjet engine; a normal shock wave interacting with the boundary layer of an airfoil operating at transonic speeds. In situations involving SWBLIs, the solid body feels a pressure increase in the direction of the flow caused by means of its inherent geometrical configuration (e.g. cavity, compression corner) or by means of an external agent (e.g. shock impingement). In any case, the pressure increase in the (outer) inviscid flow translates to a positive pressure gradient in the (inner) viscous boundary layer of the solid body, causing a flow retardation which may lead to the phenomenon of flow separation. Shock-induced separation is generally a complex, unsteady phenomenon; the source of unsteadiness is not just the incoming turbulence in the boundary layer (Ganapathisubramani, Clemens & Dolling 2007) but also the inherent separation bubble dynamics (Wu & Martin 2008). Due to the inherent unsteadiness, laminar bubbles are also observed to exhibit unsteadiness (Loth & Matthys 1995). There are very few theoretical studies concerning shock-induced separation for relatively simple steady (time-averaged), two-dimensional (2-D) flow fields (Gadd 1957; Chapman, Kuehn & Larson 1958; Stewartson & Williams 1969); scaling laws for the length of 2-D shock-induced laminar separation were obtained by integrating the triple deck formulation of the boundary layer (Burggraf 1975; Davis & Sturtevant 2000). If the shock induces boundary-layer separation, it can lead to some interesting and adverse consequences such as separation bubble unsteadiness (Clemens & Narayanaswamy 2014), thermal loads (Borovoy *et al.* 2013), performance loses and unstarts (Wagner *et al.* 2009), often requiring flow control to improve the performance of the systems where they occur. This has motivated decades of extensive studies on SWBLI, the parameters affecting them and their control (Délery & Marvin 1986; Dolling 2001; Babinsky & Harvey 2011; Clemens & Narayanaswamy 2014; Gaitonde 2015).

Among the different SWBLI situations, a particularly intriguing phenomenon of flow separation is reported to occur at the leading edge of the flat plate in a supersonic/hypersonic free stream. The earliest analysis of leading-edge/zero-boundary-layer-thickness separation in a supersonic free stream was presented by Chapman (1956) and Chapman *et al.* (1958). The theoretical predictions of the gas pressure inside the separation bubble in (1.1) agreed well the experiments, thereby giving confidence in the theoretical calculations of leading-edge separation flows. It must be noted that the predictions concern subsonic and supersonic flows for which the isentropic compression assumption at reattachment is valid. The configurations (near leading-edge compression corner/shock reflection; sharp cornered leading edge) in which supersonic leading-edge separation is expected are shown in figure 1.

The ‘tick’ configuration (cf. figure 1*a*) has received greater attention among the leading-edge separation configurations. The theoretical calculation of the heat-transfer rate in a separated laminar region was performed by Chapman (1956). The calculations considered a general zero-boundary-layer-thickness case at the position of separation, a laminar mixing layer and a low velocity (‘dead-air’) region of constant pressure and temperature enclosed by a solid surface and a viscous mixing layer. Chapman *et al.* (1958) performed theoretical analysis in order to determine the dead-air pressure in a separated region for the case of zero-boundary-layer-thickness separation. The results of the laminar

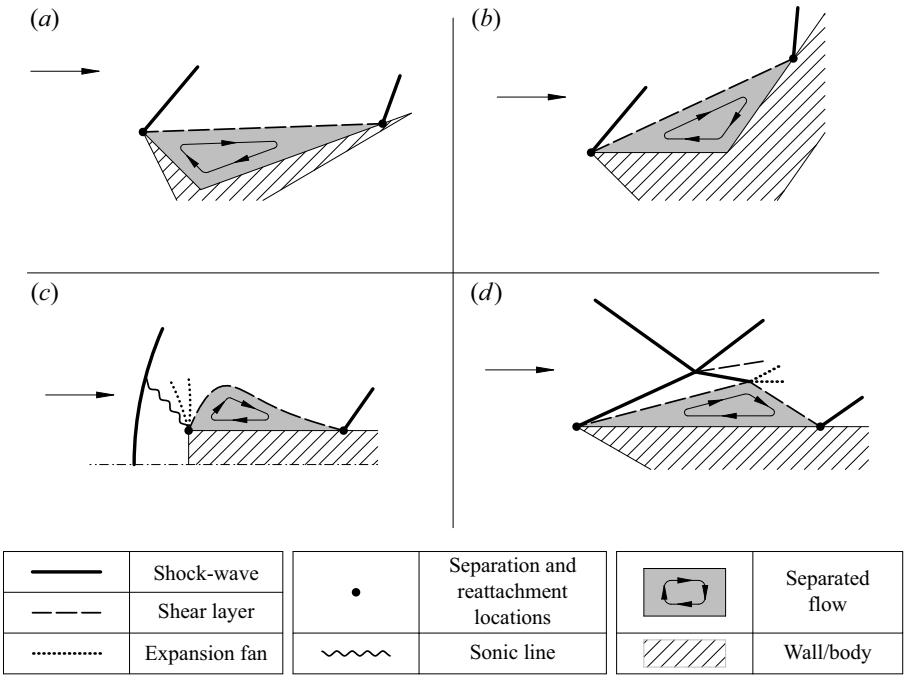

Figure 1. Schematic diagrams (not to scale) of some leading-edge separation situations in a supersonic free-stream flow: (*a*) 'tick' model; (*b*) compression corner model; (*c*) sharp-corner model; and (*d*) shock reflection model.

mixing layer theory (Chapman 1950) were used, which defined a velocity ratio $\bar{u}_*$ that is the ratio between the velocity of the dividing streamline in the laminar mixing layer and the velocity of the free-stream flow. The velocity ratio is nearly a constant $\bar{u}_* = 0.589$ and is largely independent of Reynolds number or distance from separation. Then, a mass balance argument was used in calculating the dead-air pressure: the mass flux scavenged from the dead-air zone by the mixing layer is balanced by the mass flux reversed back into the dead-air zone by the pressure rise through the reattachment zone.

A closed-form solution for the dead-air pressure (or separation pressure) p_d as a function of the static pressure p' and the Mach number M' immediately downstream of the reattachment zone was found to be

$$\frac{p_d}{p'} = \left[\frac{1 + \dfrac{\gamma - 1}{2} M'^2}{1 + \dfrac{\gamma - 1}{2} \dfrac{M'^2}{\left(1 - \bar{u}_*^2\right)}} \right]^{\gamma/(\gamma-1)}, \tag{1.1}$$

where $\gamma = 1.40$ is the specific heat ratio of air. The theoretical calculations of the dead-air pressure ratio in (1.1) were only applicable when the flow reattachment occurred through an isentropic process, typically for relatively small values of p'/p_d. The value of p_d/p' from (1.1) is found to be independent of the Reynolds number and the model shape, which agreed well with the experiments. Chapman *et al.* (1958) also introduced an efficiency factor in (1.1) which can account for non-isentropic compression, although their estimations were made only using the assumption of isentropic compression of the dividing streamline, i.e. using (1.1) as it is. However, the postulated factor is rather an

a posteriori estimate, which can only be determined after finding the relation between p_d and p'. In recent years, advancements in experimental diagnostics and computations have significantly resolved the flow over the 'tick' configuration. Strong to moderate wall cooling effects, sharp and blunt leading-edge configurations, eddy structures within the primary recirculation flow and slightly downstream displacement of the separation location from the leading edge can be found in the works of Khraibut *et al.* (2017) and Prakash *et al.* (2019). Particularly, the works by Khraibut *et al.* (2017) and Prakash *et al.* (2019) concern hypersonic separation for which the isentropic process at reattachment is not valid.

The leading-edge separation in compression corner models (cf. figure 1*b*), including those with inclined upstream walls, was investigated by Brower (1961). The flow field is analysed by the extension of laminar mixing layer theory. The theoretical investigations were carried out for a free-stream Mach number range 1–10 and compression corner angles 0°–45°. It was found that not every combination of the free-stream Mach number and the compression angle yielded a solution. Interestingly, for free-stream Mach numbers below 1.27, no leading-edge separation solution exists for any value of the compression corner angle. The lower and upper limits of the solutions are obtained for a leading-edge Mach wave and for the maximum strength of the reattachment shock. The solutions to leading-edge separation flow fields were found to be independent of the free-stream Reynolds number and had a satisfactory comparison from previous wind-tunnel experimental data.

Supersonic separated flow over a flat nosed configuration (cf. figure 1*c*) has not been studied extensively in the literature. The experiments and computations of a 2-D supersonic flow past a square-nose flat plate at Mach 1.96 were performed by Sharp (1959). The boundary layer on the frontal side of the plate is not able to negotiate the sharp right-angle corner and therefore separates, reattaching at some downstream location of the plate. From the experiments, the wall pressure measurements downstream of the square corner and the ordinates of the separation bubble and the bow wave profile were obtained. Computations were performed using the method of characteristics in the supersonic field outside the separation bubble, by treating the shear layer as a boundary line dividing the separation bubble and the outer inviscid flow. The shape of the sonic line was found to be especially sensitive in the analysis. The analysis was also applied to a rounded leading edge which was found to completely eliminate the separation bubble and the subsequent recompression.

To our knowledge, there are no detailed theoretical or experimental studies on the leading-edge flow separation caused by means of an impinging shock (cf. figure 1*d*). Despite the possibility of impinging shock-induced leading-edge separation in scenarios such as intakes at off-design Mach numbers, it has not received scholarly attention. This has motivated the present study. There is a general consensus from previous studies that the separation length increases with increasing impinging shock strength (Elfstrom 1972), decreases with free-stream Mach number (Hayakawa & Squire 1982) and increases with free-stream Reynolds number (Needham & Stollery 1966), except for the transitional boundary layer.

Délery & Marvin (1986) classified SWBLIs into 'weak' and 'strong' interactions based on the strength of the shock interacting with the boundary layer, such as the impinging shock. When the impinging shock strength is lower than the incipient pressure ratio, the SWBLI is called a 'weak' interaction. In such a scenario, the flow alterations are largely felt within the boundary layer while the external flow is unaffected, with very little

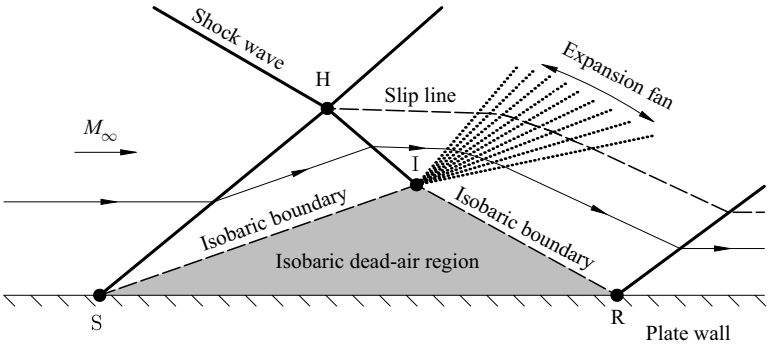

Figure 2. Schematic drawing of an inviscid flow model as described by Lees & Reeves (1964) and Green (1970), and later adopted by Délery & Marvin (1986). The model describes the separated flow caused by a 'strong' SWBLI. The locations S and R denote the locations of separation and reattachment, respectively. Note that separation does not occur at zero-boundary-layer thickness and reattachment is always parallel to the wall.

deviation from the inviscid shock reflection scenario. The boundary layer separates when the impinging shock strength is higher than the incipient pressure ratios, resulting in a 'strong' interaction. A situation occurs when the impinging shock is just strong enough for the onset of flow separation, that is, the case in which the minimum shear stress is zero; the pressure jump across the shock which is just required for the onset of separation is called the incipient separation pressure. For impinging shock strengths of the orders of incipient separation pressures, the separation lengths are found to scale with the boundary-layer thickness (Liepmann, Roshko & Dhawan 1951; Gadd, Holder & Regan 1954; Bogdonoff & Kepler 1955; Chapman *et al.* 1958; Hakkinen *et al.* 1959; Katzer 1989). However, for impinging shocks which are considerably stronger than incipient separation strength, the separation lengths could be much larger than the boundary-layer thickness. In such a case it could be possible to reduce the separated shear layer into separation lines (dividing outer flow and dead air), and treat it as an inviscid problem where we only deal with the complex wave interactions. The complex wave interactions were described in Lees & Reeves (1964) and Green (1970), and later adapted by Délery & Marvin (1986) to form an inviscid flow model (cf. figure 2). The model consists of a dead-air region having a constant pressure whose free boundary starts from the separation location. The impinging shock, modified by the interaction of the separation shock, hits the separated shear layer and reflects as an expansion fan. The expansion fan alleviates the shock pressure jump causing the free boundary of the dead-air region to end at the reattachment location. It is important to note that the separation for the case of zero-boundary-layer thickness was not considered in figure 2.

From shock tunnel experiments by Sriram & Jagadeesh (2014) and Sriram *et al.* (2016), such large separation bubbles near the leading edge, having a separation length comparable to the distance of shock impingement from the leading edge, were observed to follow a Reynolds number-independent scaling law given by

$$\frac{L}{x'}M_\infty^3 \propto \frac{p'}{p_\infty}, \tag{1.2}$$

where L is the separation length; x' and p' are the reattachment distance from the leading edge and the reattachment pressure; and M_∞ and p_∞ are the free-stream Mach number and free-stream static pressure. The 'large' separation bubbles were also observed to be

taller (based on the observed height of the shock impingement point on the separated shear layer) and had an upstream skewness (larger proportion of the bubble length being upstream of the shock impingement location on the separated shear layer) characteristic of hypersonic separated flows. The motivation behind the inviscid modelling of the leading-edge separation flow (LESF) comes from the Reynolds number-independent scaling as given in (1.2). When we have leading-edge separation, we expect the scaled separation length to always be unity (scaling with the distance of reattachment from the leading edge); this means that the scaling law effectively reduces to the inviscid relation between the pressure ratio and Mach number. This motivates us towards the possibility of an inviscid model for the shock-induced leading-edge separation.

In the present work we use a perfect fluid model to determine the pressure in the separated bubble, but this does not mean isentropic compression at reattachment, as assumed by the Chapman *et al.* (1958) model. We rather have a shock at reattachment due to which we have an entropy increase. This model is similar to the one suggested by Délery & Marvin (1986) where the reattachment pressure is equal to the inviscid shock reflection pressure.

Leading-edge separation studies can find applications in scramjet engine inlets. The air compression in the engine inlet is achieved by the generation of the ramp shock and its subsequent reflection from the cowl plate. At design conditions, the ramp shock impinges exactly at the cowl leading edge. However, at off-design conditions (higher Mach number) the shock impinges on the boundary layer developing downstream of cowl leading edge. The ramp shock–cowl plate interaction (Mahapatra & Jagadeesh 2009) typically occurs at the cowl plate leading edge, called the shock-on-lip configuration, which can cause a leading-edge separation. The present work can shed some light on the separated flow behaviour and therefore the separation bubble characteristics can be well anticipated.

In this paper, we investigate the phenomenon of shock-induced leading-edge separation in hypersonic flows, as shown in figure 3. First, in § 2, we describe the shock tunnel facility, hypersonic free-stream conditions and the test models used in the experiments. The subsequently presented results are twofold: in § 3, we construct a LESF theoretical model for the leading-edge separation. The separation bubble geometry which is constructed from three parameters: free-stream Mach number, wedge angle and the reattached flow turning angle, is detailed here. The second part of our study is presented in § 4 and focusses on the experiments involving leading-edge separation in a shock tunnel facility. Experimentally, the separation flow fields are analysed using schlieren visualizations and surface pressure measurements. The results from the LESF model are compared with the experiments, thereby validating the theoretical model. The geometric similarity of the separation flow fields is carefully looked into as the shock impingement location is moved close to the leading edge of the plate wall. The insights from the theoretical modelling and the experiments shed some light on the 'large' separation bubbles typically encountered in scramjet engine inlets.

2. Experimental facility and test models

Experiments are performed in the Hypersonic Shock Tunnel 2 (HST2) facility at the Laboratory for Hypersonic and Shockwave Research (LHSR), IISc, Bengaluru. The HST2 is a conventional shock tunnel consisting of the following components in order: a shock tube of 50 mm internal diameter, with driver and driven sections of length 2 and 5.12 m, respectively separated by a metal diaphragm; a conical divergent nozzle of fixed exit

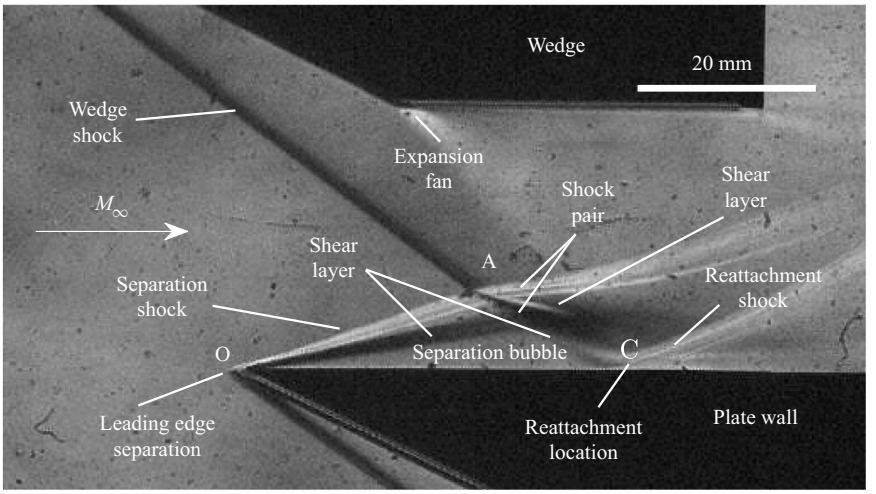

Figure 3. A schlieren photograph of a shock-induced leading-edge separation. The shock waves, expansion fans and shear layers are labelled. O, A and C denote the locations of the leading edge, shock–shock interaction and reattachment, respectively.

M_∞	5.52
P_∞ (kPa)	2.04
T_∞ (K)	182
$Re_\infty \times 10^{-6}$ (m^{-1})	4.79
H_0 (MJ kg^{-1})	1.29

Table 1. The free-stream conditions in HST2.

diameter of 300 mm, and replaceable throat section between the nozzle and shock tube (which fixes the Mach number); a test section of 450 mm length and 300 mm × 300 mm square cross-section; and a dump tank of $2\,m^3$ volume. The end of the shock tube is fitted with two piezoelectric pressure sensors which are used to measure the reservoir flow properties of the shocked air prior to the nozzle entry. The end of the shock tube and the nozzle entry are separated by a paper diaphragm. A Pitot pressure measurement at the test section and the reservoir pressure measurement at the shock tube end are used to characterize the free-stream conditions in HST2. Furthermore, the test section is installed with transparent glass windows on either side such that flow visualizations (e.g. schlieren, shadowgraphy) over the test models can be performed. The detailed working of the HST2 can be found in the works of Sriram (2013) and Srinath (2015). The free-stream conditions for the present experiments are shown in table 1. We also validate the free-stream Mach number and static pressure by measuring the wedge angle, wedge shock angle and the dead air pressure in the experiments, details of which are given in Appendix A.

We remark that the Pitot rake measurements by Kulkarni (2007) and Mahapatra (2010) in HST2 showed that the diameter of the core flow was larger than the model diameter (typically approximately 100 mm) and that the stagnation pressure was constant in this region. Therefore, the length scales of the models (i.e. wedge and flat plate) and their positions relative to the nozzle exit are such that the free stream is not significantly affected by the conicity of the flow. The free-stream uncertainties are estimated following the

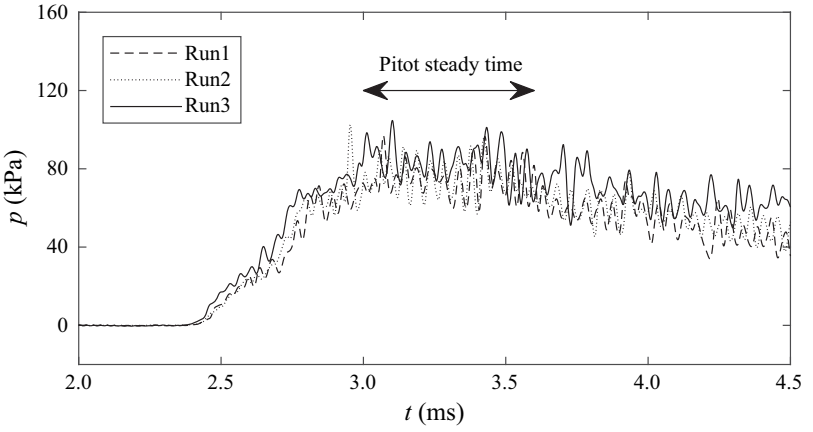

Figure 4. The pressure signals from a Pitot probe mounted in the test section. The three signals are shown here to illustrate repeatability.

methodology of Moffat (1988). They are calculated to be $\pm 1.86\,\%$ in free-stream Mach number, $\pm 6.54\,\%$ in free-stream static pressure, $\pm 6.07\,\%$ in static temperature, $\pm 9.71\,\%$ in free-stream unit Reynolds number and $\pm 6.54\,\%$ in total enthalpy. The detailed uncertainty calculations can be found in the work of Srinath (2015). Here, it must be stated that, at low enthalpies of $H_0 \approx 1\,\mathrm{MJ\,kg^{-1}}$, high-temperature effects (e.g. dissociation, chemical reactions) in air are not expected to occur. Under the present experimental conditions, the STN code (Shock Tube Nozzle calculations for equilibrium air by Krek & Jacobs 1993) estimates an insignificant change in the specific heat ratio of the free-stream air ($\gamma \approx 1.40$), which suggests air behaves as an ideal gas at the enthalpies at which the present studies were conducted.

The Pitot signals are shown in figure 4. It is observed that the test time is around 600 µs (between 3.0 and 3.6 ms in figure 4), and the different signals demonstrate repeatability. Since the test times are extremely short, the time resolution of the separated flow field is very crucial. The evolution of the shock-induced large separated flow field within the short shock tunnel test time was discussed by Sriram *et al.* (2016). It was reported that within around 300 µs after a steady free stream is established, a statistically steady separated flow field evolved. Hence, the steady separated flow measurements can be performed within the 600 µs available steady free stream. The steady separated flow features can be verified in the transient pressure signals on the plate wall (cf. figure 18) and the schlieren time evolution of flow field (cf. figure 19) plots.

The test models used in the present experiments are: a wedge (impinging shock generator) of angle 26.6° relative to the free-stream direction and a plate wall of length 200 mm having a sharp leading edge (bluntness radius $r_b < 0.1$ mm). The wedge and the plate wall each have a span of 120 mm. Figure 5 shows photographic images of the test models used. The effects of model span, for both the wedge and the flat plate, on the separated flow field are given in Appendix D. The wedge and the plate are held in their respective positions as shown in figure 6 with the use of a fixture. A vertical gap of 30 mm is maintained between the wedge and the plate wall for the air flow. Larger vertical gap distances tend to curve the (impinging) wedge shock before its impingement. Smaller vertical gap distances could result in multiple shock reflections with the wall or shear layer on the top, resulting in complex system of shocks and back pressure fluctuations. The horizontal positions of the plate leading edge, relative to the wedge

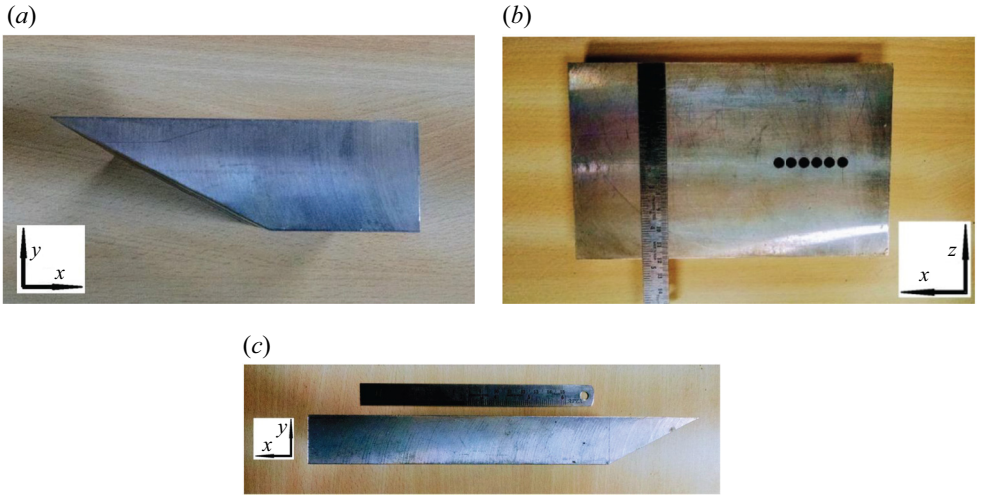

Figure 5. Photographs of the test models used in the present study. (a) Side view of the wedge; (b) top view of the plate wall; (c) side view of the plate wall.

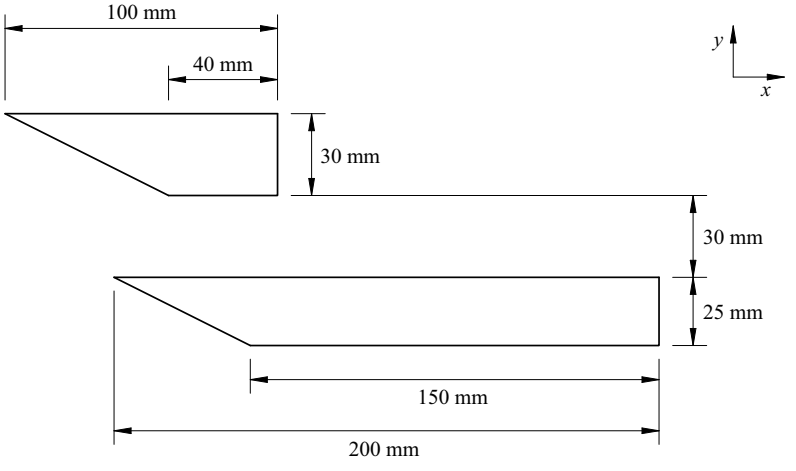

Figure 6. Two-dimensional drawing of a typical model arrangement. Wedge (top) and plate wall (bottom) are the test models used, each having a span of 120 mm (not shown in the figure).

leading edge, are chosen in the range 10–60 mm so as to attain leading-edge separation flows. Since the relative vertical gaps of the models are fixed, the model configurations are solely determined by the horizontal positions. Consequently, the configurations are named corresponding to the inviscid shock impingement locations from the plate leading edge, denoted by X_{ir} (cf. figure 24). For example, if a model configuration produces a (inviscid) shock impingement around 40 mm from the plate leading edge, it will be referred to as the $X_{ir} \approx 40$ mm configuration. The subscript 'ir' refers to inviscid (shock) reflection. We also perform experiments with a wedge of angle 21.80° at nominal Mach numbers of 6 and 8 to further validate the LESF model.

Time resolved surface pressure measurements are carried out using piezoelectric pressure sensors (uncertainty of $\pm 1\,\%$) which are flush mounted along the centreline of the plate wall. The pressure sensor centres are placed at 30, 38, 46, 54, 62 and 70 mm from

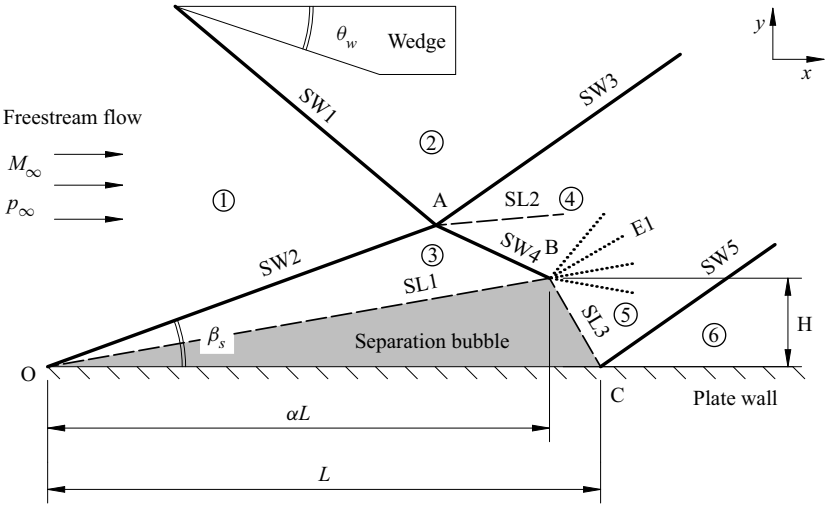

Figure 7. Schematic drawing (not to scale) of the LESF model. The model describes a 2-D steady state inviscid flow field over the plate wall. Regions 2–6 are obtained after passing through a combination of shock (thick lines), expansion (dotted lines) and/or slip lines (dashed lines). The separation bubble △OBC is characterized by the bubble pressure p_d, the separation length L, the upstream skewness α and the separation height H.

the leading edge of the plate. Some experiments are also performed with Kulite pressure sensors (uncertainty of $\pm 0.5\,\%$) measuring wall pressures at 15 mm from the leading edge of the plate. The sensors, which are flush mounted to the plate wall, connect externally to a data acquisition system (by National Instruments) operating at 1 MHz. The flow field in the test section is visualized using a z-type schlieren arrangement (Settles 2001) using a high-speed Phantom V310 camera operating at 20 kHz with a spatial resolution of 518 px × 288 px. The pixel resolution in the schlieren images was around 0.18 mm. The schlieren visualizations are configured with a horizontal knife edge which is used to resolve vertical gradients in the flow.

3. Modelling

Figure 7 illustrates the LESF model whose motivation comes from the Reynolds number independence of our previous scaling laws (Sriram & Jagadeesh 2014; Sriram *et al.* 2016) and from a separated flow model from previous literature (Délery & Marvin 1986). We remark that the LESF model developed in the present study is very similar to the inviscid model of Délery & Marvin (1986) (cf. figure 2), except that (i) in our case we consider a hypersonic Mach number as opposed to a supersonic Mach number in their case, (ii) we consider flow separation at the leading edge and (iii) we consider the possibility of 'normal' flow (through a normal shock) at reattachment.

3.1. *Theoretical framework*

In the LESF model, a wedge of angle $\theta_w > 0^\circ$ is placed in a free-stream flow (cf. figure 7); Mach number $M_1 = M_\infty$, static pressure $p_1 = p_\infty$ and flow direction $\theta_1 = 0^\circ$; where it generates a wedge shock SW1.

The shock SW1 is of strength (static pressure jump) p_2/p_1 and deflects the free-stream flow from θ_1 to $\theta_2 = -\theta_w$ towards a plate wall. The shock SW1 causes a SWBLI over the plate wall which results in the flow separation at the leading-edge location O.

The leading-edge separation causes generation of a separation shock SW2 and a slip line SL1 at location O.

The shock SW2 is of strength p_3/p_1 and deflects the free-stream flow from θ_1 to θ_3 away from the plate wall. Here, the separation shock angle is denoted by β_s and the slip line by $\theta_s = \theta_3$. A slip line is a dividing streamline which allows tangential velocity jumps while maintaining the local flow direction and static pressure values across its boundary (a concept previously used in the works of Chapman *et al.* 1958; Délery & Marvin 1986).

The slip line SL1 divides the supersonic flow in region3 from a dead gas flow in the separation bubble. The static pressure in the separation bubble is constant given by $p_d = p_3$.

Downstream of the flow, a Type-I shock–shock interaction (refer to Edney (1968) for shock–shock interactions) is assumed between the shock SW1 and shock SW2, which meet at point A and the formation of two additional shocks SW3 and SW4 and a slip-line SL2 ensues. The slip line SL2 maintains the local flow direction θ_4 and the local static pressure value p_4 while having tangential velocity jumps across its boundary.

The shock SW4 interacts with the separation bubble $\triangle$OBC at location B to result in an expansion fan E1, turning SL1 towards the plate. The turned slip line is denoted as SL3. The constant pressure condition in the separation bubble $\triangle$OBC is the reason for the shock SW4 to reflect as an expansion fan E1, and therefore turn the slip line SL1 into SL3 in the direction of the wall.

The slip line SL3 divides the supersonic flow in region5 from the dead gas flow in the separation bubble while maintaining the static pressure $p_5 = p_d$ across its boundary. The slip line SL3 meets the wall at location C and disappears. As the supersonic flow in region 5 approaches the plate wall, a reattachment shock SW5 forms at location C, which aims to change the flow direction parallel to the wall. The (apparent) point of intersection between the slip line SL3 and the shock SW5 is the reattachment location C.

Immediately downstream of the reattachment location C, the plate wall experiences a large reattachment pressure $p' = p_6$ acting over it, and this jump in pressure to peak values signifies the re-attachment of the separated flow. This large reattachment pressure continues to be felt downstream of the reattachment location unless perturbed by other wave interactions/viscous layers (e.g. expansion fan from the wedge, growing boundary layer of the plate wall). In the LESF model, we investigate the flow field from the plate leading edge up to immediately after the reattachment location and detail the structure of the SWBLI (see figure 7) for a leading-edge separation situation.

3.2. *Reattachment flow fields: oblique and normal*

The reattachment of the flow is crucial in the LESF model. Figure 8 shows two reattachment flow fields: oblique ($\kappa = 0$) and normal ($\kappa = 1$), where κ is a Boolean variable that is either 0 or 1. The terms oblique and normal reattachment should be interpreted as oblique shock and normal shock reattachment.

In an oblique reattachment (cf. figure 8*a*), the flow is supersonically turned parallel to the wall by a planar reattachment shock SW5. However, in a normal reattachment (cf. figure 8*b*), the flow is not able to turn large angles and a detached bow shock SW5 occurs. Downstream of this bow shock, the flow is subsonically turned parallel to the wall. Importantly, the bow shock in the immediate vicinity of the reattachment location C behaves like a normal shock. The detachment distance (i.e. the shock stand-off distance of the bow shock SW5) and the pressure variations in the subsonic region of the bow shock are ignored in the present analysis.

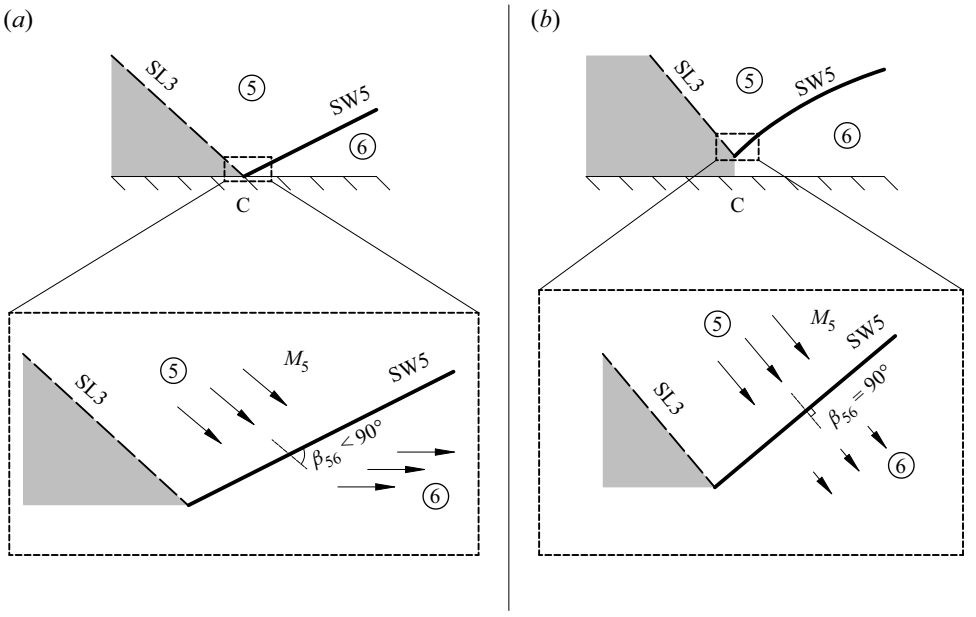

Figure 8. Schematic drawings (not to scale) of the two reattachment flow fields: (*a*) oblique ($\kappa = 0$) and (*b*) normal ($\kappa = 1$) reattachment. For the case of a normal reattachment, the bow shock behaves as a normal shock in the close vicinity of location C. Note that the schematic drawings are only simplifications of real flows near reattachment.

The static pressure in regions 5 and 6 are important parameters for flow reattachment. Note that the static pressure in region 5 is equal to the dead-air pressure of the separation bubble, i.e. $p_5 = p_d$ and the static pressure in region 6 is called the reattachment pressure, i.e. $p_6 = p'$. They are related by the oblique shock relation

$$\frac{p'}{p_d} = \frac{2\gamma\,(M_5 \sin\beta_{56})^2 - (\gamma - 1)}{(\gamma + 1)}. \tag{3.1}$$

Here, M_5 is the Mach number in region 5 and β_{56} is the angle of the reattachment shock relative to the oncoming flow in region 5. Note that M_5 and β_{56} are only functions of γ, M_∞, θ_w and p_d/p_∞ resulting from solving two oblique shocks (SW2 and SW4) and an expansion fan (E1) between regions 1, 3, 4 and 5 (cf. figure 7). Therefore, (3.1) essentially gives a relation between the separation pressure p_d and the reattachment pressure p', which must be solved numerically since there is no closed-form solution. We form a relation between p_d and p' in (3.1) as was done before by Chapman *et al.* (1958) in (1.1), except that the present scenario concerns the case of non-isentropic compression at reattachment. This is indeed a critical difference between the present approach and the theory by Chapman *et al.* (1958). The theory by Chapman *et al.* (1958) considers isentropic recompression of the dividing streamline, imposing the boundary-layer theoretical consideration that the outer flow static pressure at reattachment is the same as total pressure of the dividing streamline. In relating the dead-air pressure with the outer flow conditions after reattachment, the theory assumes isentropic compression of all streamlines, including those in the outer flow. However, at hypersonic Mach numbers this is not the case. In the present model, based on the inviscid picture by Délery & Marvin (1986), the calculations only concern the outer inviscid flow; the entire outer flow at the reattachment location is turned by a reattachment shock which is a non-isentropic phenomenon, and thus p_d and p'

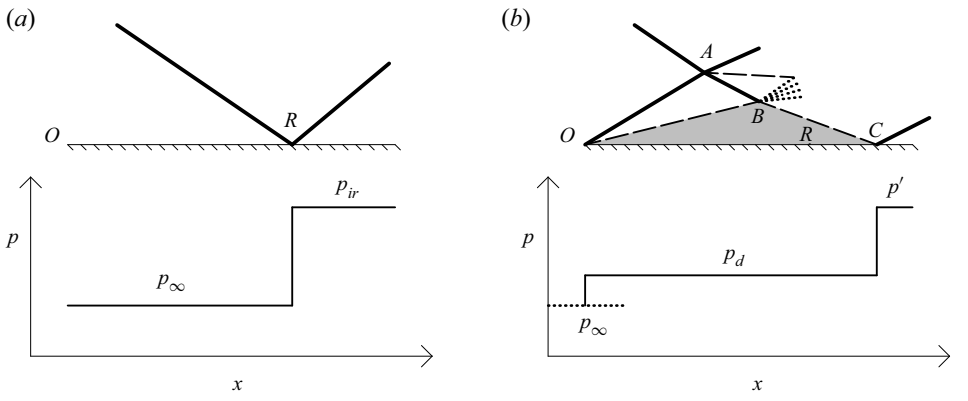

Figure 9. Schematic diagram (not to scale) and wall pressure profiles of (*a*) unseparated and (*b*) separated flows. The unseparated flow is characterized by the pressure jump p_{ir}/p_∞ and the shock impingement distance $X_{ir} = OR$. The separated flow is characterized by the pressure jumps p_d/p_∞ and p'/p_d, and the separation length $L = OC$.

are related using shock relations. We remark that, for a normal reattachment, β_{56} is always equal to 90°.

The occurrence of an oblique or a normal reattachment depends on the strength of the wedge shock. For wedge shocks of low strength i.e. low p_2/p_∞, an oblique reattachment is expected because the reattachment pressures ratios are relatively low i.e. low p'/p_∞. However, as the wedge shock strength increases, we expect a transition to a normal reattachment where the reattachment pressure ratios are relatively high. The experimental observation of 'large' separation bubbles and a detached shock at reattachment that is strongly curved near the wall was reported by Sriram (2013), Sriram & Jagadeesh (2014, 2015), Srinath (2015) and Sriram *et al.* (2016). It was hypothesized that the flow upstream of reattachment sees a small normal reattachment shock region which can cause large reattachment pressure ratios.

We note that, for intermediate wedge shock strengths, a near-sonic reattachment, i.e. $M_6 \approx 1$, would occur where the flow downstream of the reattachment shock is at the attached–detached transition of the reattachment shock. Since the LESF model can produce a dual solution in some cases i.e. an oblique and normal reattachment, we will rely on experimental evidence to determine the correct solution.

We emphasize that, in real flows, the reattachment is a complex process. The reattachment shock is always detached from the plate wall and is curved at the location of reattachment. This is due to the interactions between viscous layers and shear layers at the location of reattachment, which cannot be captured in the LESF model.

3.3. *Methodology*

In figure 9 we contrast the flow fields and pressure distributions of separated and unseparated flows. For the unseparated flow (cf. figure 9*a*) there are two characteristic parameters: the shock impingement distance $OR = X_{ir}$ and the inviscid shock reflection pressure ratio p_{ir}/p_∞. However, for the separated flow (cf. figure 9*b*), there are three characteristics parameters: the separation bubble length $OC = L$, dead-air pressure ratio p_d/p_∞ and reattachment pressure ratio p'/p_d.

The central goal of the LESF model is to determine p_d/p_∞ (or equivalently the separated shock angle β_s), so that the geometry of the separation bubble $L/X_{ir}, H/L, \alpha$ can be

easily computed. Since p_d is related to p' in (3.1), a criterion for p' must be fixed. We assume that the reattachment pressure for the separated flow is equal to the inviscid shock reflection pressure, i.e. $p' = p_{ir}$. The details on p_{ir} are provided in Appendix B. This approximation of the pressure ratio at reattachment is supposedly a valid assumption for 'weak' shocks where p_2/p_1 is relatively small, as described in the literature (Liepmann *et al.* 1951; Gadd *et al.* 1954; Chapman *et al.* 1958; Hakkinen *et al.* 1959; Brower 1961; Stollery & Bates 1974; Délery & Marvin 1986; Katzer 1989; Délery & Dussauge 2009). For 'strong' shocks, where p_2/p_1 is relatively large, the reattachment pressure ratio is observed to be lower but of the same order as that of the inviscid shock reflection pressure ratio (Mallinson, Gai & Mudford 1997; Matheis & Hickel 2015; Verma & Chidambaranathan 2015).

Following this, we again state the assumptions in the LESF model:

(i) The flow separation occurs at the leading edge of the plate wall.
(ii) The reattachment pressure ratio approximately equals the inviscid shock reflection pressure ratio, $p'/p_\infty \approx p_{ir}/p_\infty$.
(iii) The interaction between the wedge shock SW1 and the separation shock SW2 is a Type I interaction.
(iv) The working gas is calorically perfect (constant C_p and C_v everywhere).

Figure 10 shows the flow chart of the iterative method used to calculate flow quantities in uniform regions in figure 7. Appendix C shows the oblique and normal reattachment solutions to a small range of impinging shocks over a plate wall in an air flow. Here, it must be stated that, although the LESF model does not account for any viscosity effects, in real flow situations, separation is a viscous effect. We paraphrase this statement from Brower (1961) since his research also involved leading-edge separation flow fields but over compression corners. For leading-edge separation flows, the separated flow field interestingly happens to be viscosity independent (or equivalently Reynolds number independent) since the complicated development of the boundary layer (e.g. laminar to turbulent boundary-layer transition) and its associated pressure variations from plate leading edge to separation location may be avoided. Previous works on leading-edge separation flows by Chapman *et al.* (1958), Brower (1961) and Srinath, Sriram & Jagadeesh (2017) show geometrically similar flow fields and an independence of free-stream Reynolds number. We remark that the structure of two separated flows is said to be geometrically similar if it can be perfectly matched by simply enlarging or reducing the geometry.

3.4. *Solution range*

For a fixed Mach number, the LESF model allows solutions only within a limited range of wedge angles. The minimum wedge angle is obtained when either the separation/reattachment is a Mach wave and the maximum wedge angle is obtained when a possible Type II interaction occurs between the wedge shock and the separation shock (cf. table 2).

The LESF model cannot admit wedge angles smaller than $\theta_{w,min}$ since the separation/reattachment shock strength cannot be lower than that of a Mach wave. For the maximum value, we limit the wedge angles by $\theta_{w,max}$ at which a Type I to Type II transition can possibly occur between the wedge shock and the separation shock. An estimate of $\theta_{w,max}$ is obtained from the shock polar plots which are commonly used to quantify shock–shock interactions. Figure 11 shows examples of wedge shock–separation

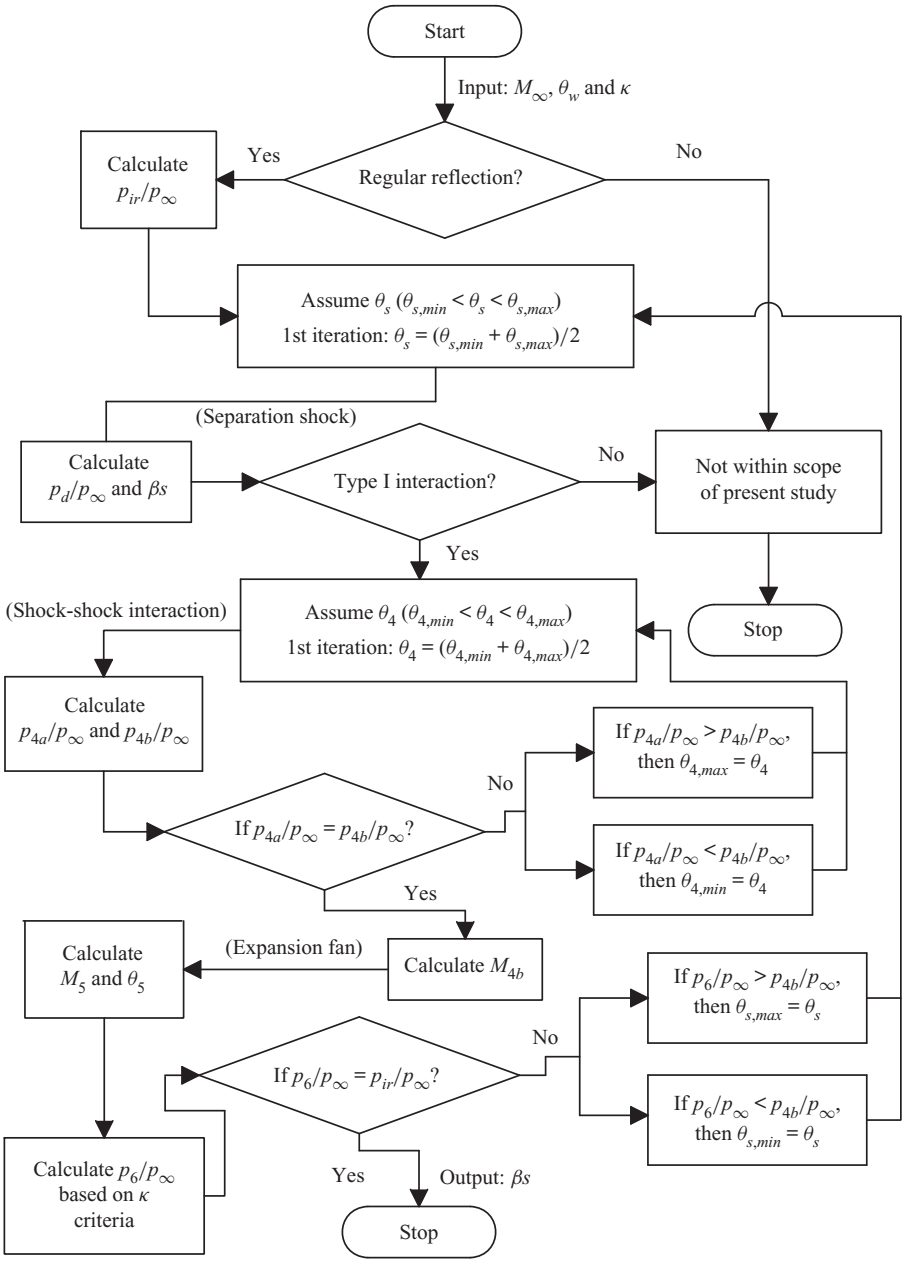

Figure 10. Double iterative algorithm for solving the separation shock angle in the LESF model. Input parameters are M_∞, θ_w and κ. The output parameter is β_s, which determines the separation bubble parameters (e.g. p_d/p_∞, L/X_{ir}, H/L). Note that regions 4*a* and 4*b* denote the regions above and below the slip line SL2 in figure 7, respectively. In the calculations, $\gamma = 1.40$ is fixed, which corresponds to air flows.

shock interactions at free-stream Mach 5. The interaction for minimum and maximum wedge angles for an oblique reattachment is shown in figures 11(*a*) and 11(*b*). And figures 11(*c*) and 11(*d*) are similar plots for a normal reattachment. The locus line plot is shown in figure 11(*e*), which spans the solution for all possible wedge shock–separation shock interactions for an oblique and a normal reattachment. The locus lines begin at $\theta_w = \theta_{w,min}$

θ_w	$\kappa = 0$	$\kappa = 1$
$\theta_{w,min}$	$p'/p_d = 1$	$\beta_s = \sin^{-1}\left(\frac{1}{M_\infty}\right)$
$\theta_{w,max}$	Type II	Type II

Table 2. Criteria at minimum and maximum wedge angles. Here, Type II refers to the nature of interaction between the separation and the wedge shock.

and end at $\theta_w = \theta_{w,max}$. The maximum wedge angle $\theta_{w,max}$ is defined at the triple point i.e. when the wedge shock polar, separation shock polar and the free-stream shock polar intersect at a single point. We do not consider solutions outside of the free-stream shock polar as they would possibly lead to a Type II interaction (Sriram *et al.* 2016) where the LESF model would not work.

Figure 12 shows the plots of the minimum, maximum and detached wedge angles which are functions of free-stream Mach number. The detached wedge angle θ_w^D is another critical wedge angle which marks the transition between the regular–irregular reflection on a plate wall (cf. Appendix B). In figure 12, we find that $\theta_{w,max} < \theta_w^D$. Furthermore, a region in the range $16^\circ < \theta_w < 19^\circ$ is identified where no oblique/normal solution exists. We suppose that the wedge angles are intermediate in this region resulting in neither a 'weak' nor a 'strong' impinging shock. A near-sonic reattachment is very likely to occur in this region which is thought to transition towards a normal reattachment.

3.5. *Separation bubble characteristics*

The separation bubble in the LESF model is characterized by the dead gas pressure p_d, separation length L, upstream skewness α and separation height H. An important feature of the LESF model is the geometrical similarity of the SWBLI. Since the separated flow variables (e.g. p_d/p_∞, β_s, L/X_{ir}) depend only on inviscid flow variables (e.g. M_∞, θ_w), the resulting leading-edge separation flows are expected to be geometrically similar and hence do not depend on the location of shock impingement X_{ir}. The consequence of this is that the leading-edge separated flows are Reynolds number independent.

3.5.1. *Oblique reattachment* $\kappa = 0$

Figure 13 shows the separation bubble characteristics for the case of an oblique reattachment. Here, we remark that the flow immediately downstream of the reattachment shock (region 6 in figure 8*a*) is typically supersonic. When the wedge angle tends to its minimum value $\theta_w \to \theta_{w,min}$, we find that $p'/p_d \to 1$, that is, the reattachment shock tends to a Mach wave, while $p_d/p_\infty > 1$, that is, the separation shock is stronger than a Mach wave. This necessarily means near zero flow deflection across the reattachment shock, resulting in an open separation $L/X_{ir} \to \infty$. And since $p_d/p_\infty > 1$, we have a finite H/X_{ir} and thus $H/L \to 0$. That is to say, we have an open and shallow separation when $\theta_w \to \theta_{w,min}$. We remark that this extreme geometry is a theoretical limit when the reattachment shock tends to a Mach wave. However, as the wedge angle increases, we see that the separation and reattachment shock strengths gradually increase with the condition that the separation shock strength is always greater than the reattachment shock strength $p_d/p_\infty > p'/p_d$. The open and shallow separation bubble is gradually relieved

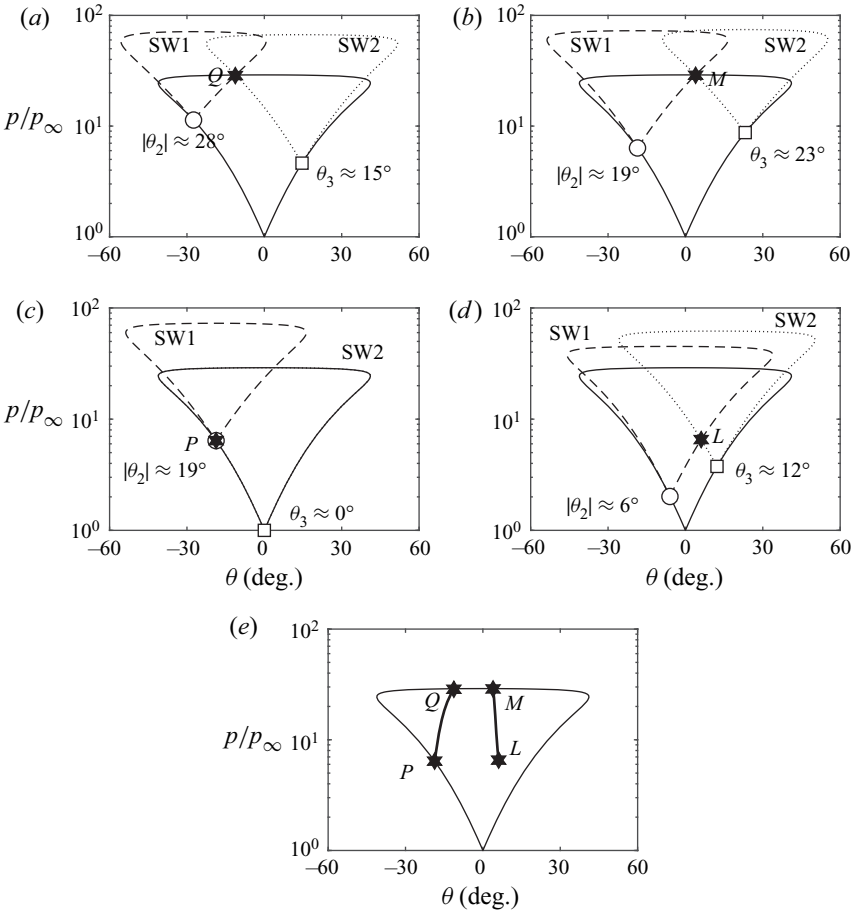

Figure 11. Shock polar plots of SW1–SW2 interactions. SW1, SW2 and free-stream shock polars are indicated by dashed, dotted and continuous (thin) lines. The wedge angles are indicated by open circles, the separation shock angles by open squares and the SW1–SW2 shock polar intersections by black stars. (*a*,*c*) The interactions at $\theta_{w,min}$ and $\theta_{w,max}$ at $\kappa = 1$. (*b*,*d*) The interactions at $\theta_{w,min}$ and $\theta_{w,max}$ at $\kappa = 0$. (*e*) The locus of the SW1–SW2 interactions is denoted by LM and PQ (thick lines) for $\kappa = 0$ and $\kappa = 1$ respectively. The coordinates at each point in either LM or PQ denote the flow deflection and the pressure ratio in region 4 (cf. figure 7). For all cases in this figure, $M_\infty = 5$.

as the wedge angle increases since the reattachment shock strength gradually increases. When the wedge angle tends to the maximum value $\theta_w \to \theta_{w,max}$, the separation and reattachment shocks strengths reach their respective maximum values while a stabilization occurs in the separation bubble geometry. The stabilization can be seen in figures 13(*c*), 13(*d*) and 13(*e*) where a gradual collapse of the curves occurs near the maximum wedge angle. When the wedge angles are greater than the maximum value $\theta_w > \theta_{w,max}$, we would expect a gradual transition to a near-sonic reattachment.

3.5.2. *Normal reattachment* $\kappa = 1$

Figure 14 shows the separation bubble characteristics for a normal reattachment. When the wedge angle tends to its minimum value $\theta_w \to \theta_{w,min}$, we find that $p_d/p_\infty \to 1$, that is, the separation shock tends to a Mach wave, while $p'/p_d \gg 1$, that is, the reattachment

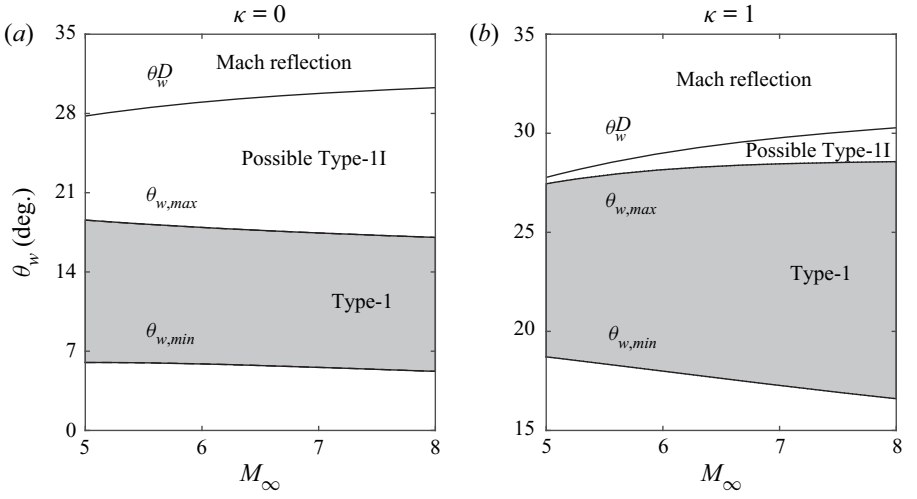

Figure 12. Plots of critical wedge angles $\theta_{w,min}$, $\theta_{w,max}$ and θ_w^D as a function of M_∞ for (*a*) $\kappa = 0$ and (*b*) $\kappa = 1$. The shaded grey regions show the range of wedge angles where solutions to the LESF model exist.

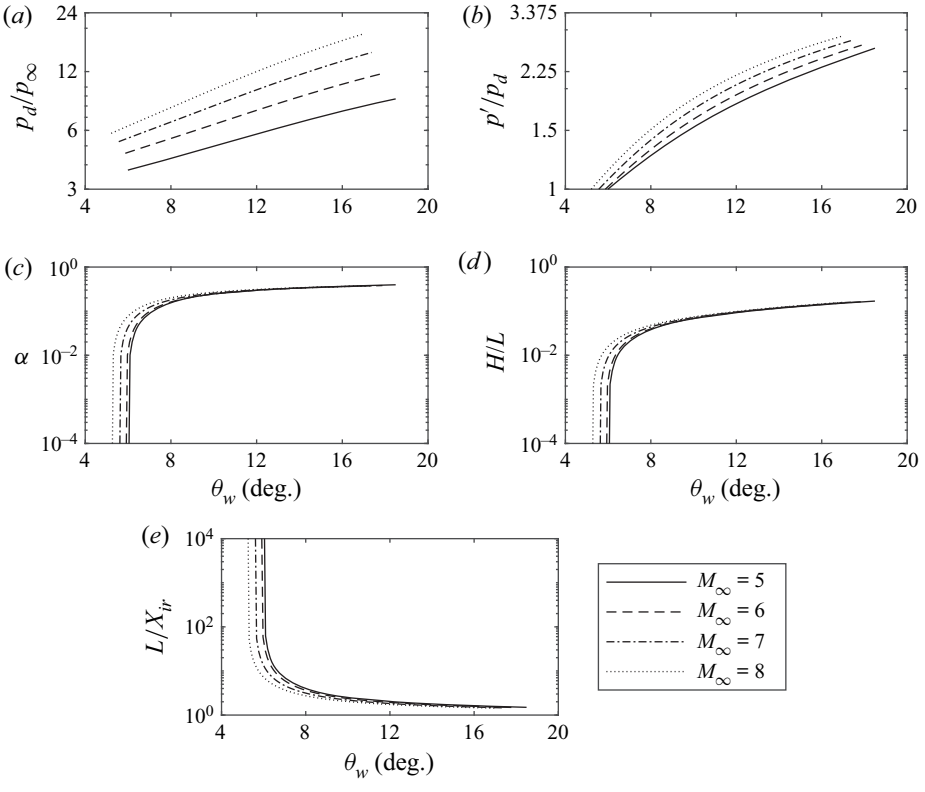

Figure 13. Separation bubble characteristics for an oblique reattachment $\kappa = 0$. Plots of (*a*) p_d/p_∞, (*b*) p'/p_d, (*c*) α, (*d*) H/L, (e) L/X_{ir} as a function of θ_w.

shock strength is relatively high. This necessarily means near zero flow deflection across the separation shock, and thus a shallow separation $H/L \to 0$. Here, we do not find an open separation since $p'/p_d \gg 1$, that is, the flow upstream of the reattachment is directed

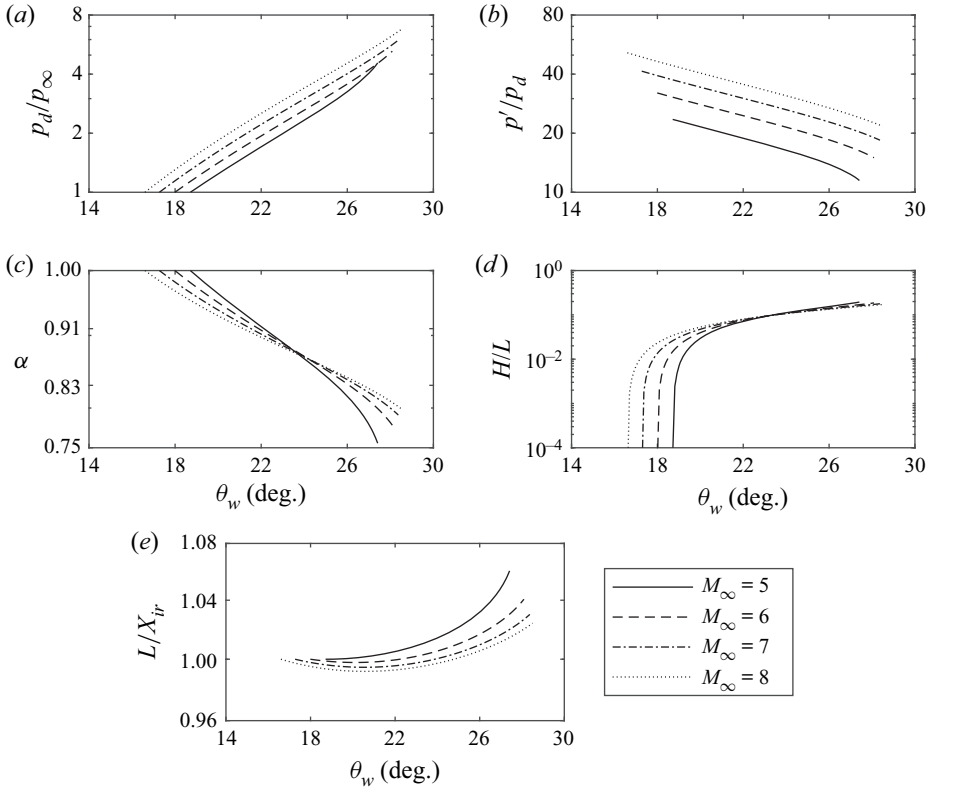

Figure 14. Separation bubble characteristics for a normal reattachment $\kappa = 1$. Plots of (*a*) p_d/p_∞, (*b*) p'/p_d, (*c*) α, (*d*) H/L, (*e*) L/X_{ir} as a function of θ_w.

towards the plate wall. Again, this extreme geometry is a theoretical limit, but for the case when the separation shock tends to a Mach wave. However, as the wedge angle increases, we see that the separation shock strength increases while the reattachment shock strength decreases with the condition that separation shock strength is always lower than the reattachment shock strength $p_d/p_\infty < p'/p_d$. The extreme geometry of the separation bubble is gradually relieved as the wedge angle increases since the separation shock strength gradually increases. When the wedge angle tends to the maximum value $\theta_w \to \theta_{w,max}$, the separation shock reaches its respective maximum value while the reattachment shock reaches its respective minimum value. The separation bubble does not stabilize at the maximum wedge angle, since variations can be seen in figures 14(*c*), 14(*d*) and 14(*e*) near the maximum wedge angle. An important feature of the normal reattachment is that it depicts the separation bubble length nearly equal to the shock impingement location from the leading edge $L/X_{ir} \approx 1$.

4. Experiments

Figure 15 shows the schlieren images of the steady SWBLIs at Mach 5.52 with a 26.6° wedge for various shock impingement locations on the flat plate (given in terms of distance from leading edge). There are a number of observations that can be made from the figure and we discuss each of them separately.

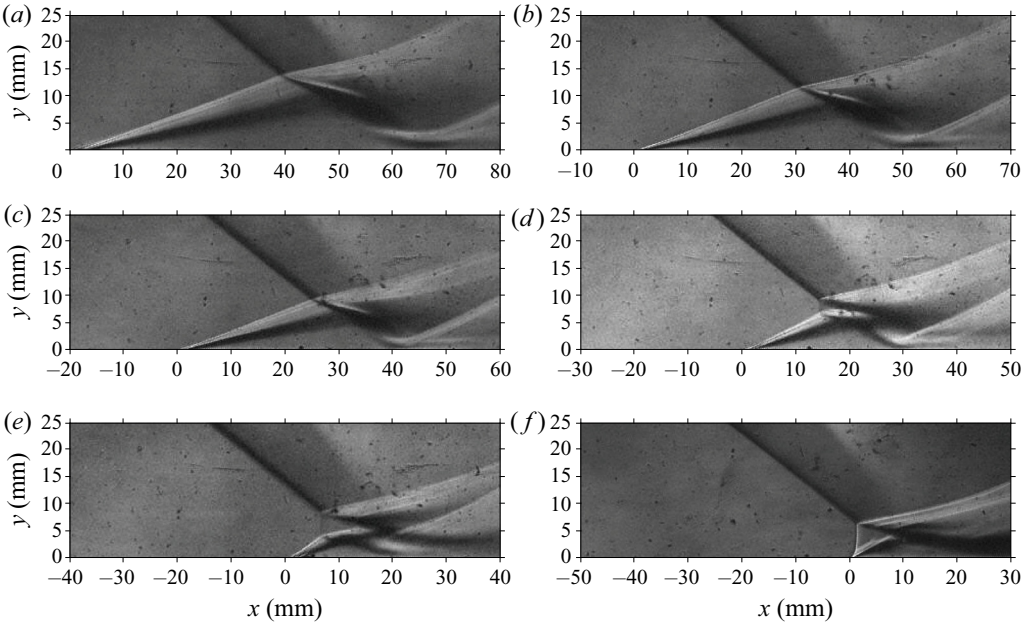

Figure 15. LESF fields at Mach 5.52 with 26.6° wedge. The shock impingement location is varied in the range 10–60 mm from the plate leading edge: (*a*) $X_{ir} \approx 60$ mm; (*b*) $X_{ir} \approx 50$ mm; (*c*) $X_{ir} \approx 40$ mm; (*d*) $X_{ir} \approx 30$ mm; (*e*) $X_{ir} \approx 20$ mm; (*f*) $X_{ir} \approx 10$ mm.

4.1. *Incipient vs 'large' separation*

From the inviscid calculations, the peak pressure ratio imposed on the plate wall due to the shock impingement is estimated to be around 55 (cf. figure 25). The severity of this imposed pressure ratio can be understood in relation to the incipient pressures necessary to separate the flow. We evaluate the typical values of the incipient separation pressures in our experiments. For this we assume that the shock impingement occurs in the range $X_{ir} \approx$ 10–60 mm, as in the present experiments. We then use the expression for the boundary-layer thickness (Hayes & Probstein 1959) which is given by (4.1)

$$\frac{\delta}{x} \sim \frac{\gamma - 1}{2} \frac{M_\infty^2 \sqrt{C_\infty}}{\sqrt{Re_{x,\infty}}}, \tag{4.1}$$

where δ is the boundary-layer thickness at a distance x from the plate leading edge, C_∞ is the Chapman–Rubesin constant which is estimated using a Sutherland's law viscosity model at wall and free-stream locations and is of order $C_\infty \sim 1$ and $Re_{x,\infty}$ is the Reynolds number based on free-stream conditions and the distance x from the plate leading edge. Please note that (4.1) is the boundary-layer growth expression in the absence of shock impingement. Using (4.1) we evaluate the incipient pressure. The expression for the incipient pressure (Délery & Marvin 1986) is given by (4.2)

$$\frac{\mathcal{P}}{p_\infty} \sim 1 + \mathcal{F}\gamma \frac{M_\infty^2}{\sqrt[4]{M_\infty^2 - 1}} \sqrt{\frac{C_f}{2}}, \tag{4.2}$$

where $\mathcal{P}$ is the pressure at the onset of separation, $\mathcal{F}$ is the universal correlation function which for laminar flows is of order $\mathcal{F} \sim 1$ and C_f is the skin friction which depends on

Incipient	Present experiments
$p'/p_\infty \sim \mathcal{P}/p_\infty \sim 2$	$p'/p_\infty \sim p_{ir}/p_\infty \approx 55$
$L \sim \delta \sim 0.3$–0.7 mm	$L \sim X_{ir} \approx 10$–60 mm

Table 3. Imposed pressure ratios and separation length scales for the incipient situation and present experiments. The δ and $\mathcal{P}$ values are evaluated at $x = X_{ir} \approx 10$–60 mm.

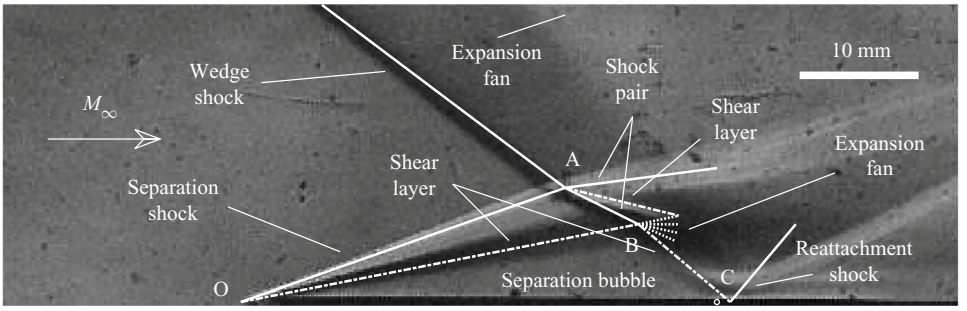

Figure 16. Comparison of the separation bubble geometry between the experiments and the LESF model. The shock pair is a result of the wedge shock and separation shock interactions. The location of the leading edge of the plate and the location of the reattachment are marked O and C, respectively. The model assumes $\kappa = 1$. In the figure, $M_\infty = 5.52$, $\theta_w = 26.6^\circ$ and $X_{ir} \approx 40$ mm.

the boundary-layer thickness, analogous to the skin friction coefficient obtained through the (laminar) Blasius solution. We summarize the orders of magnitude of relevant pressure ratios and length scales in table 3.

Even with hypersonic Mach numbers and high skin friction near the leading edge, the shock is orders of magnitude stronger than the incipient separation pressure at impingement locations. The LESF model results have already shown 'large bubbles' which are of length comparable to the distance of shock impingement, similar to what was reported previously by Sriram & Jagadeesh (2014, 2015) and Sriram *et al.* (2016).

The present experiments also showcase such 'large bubbles' for strong impinging shocks. The lengths of the 'large bubbles' are experimentally determined simply by locating the reattachment. The methodology to obtain the reattachment locations is detailed by Sriram *et al.* (2016). The uncertainty in the reattachment location is ± 2.5 mm.

4.2. *Separation bubble geometry*

Interestingly, the separation bubble geometries at $X_{ir} \approx 60$, 50 and 40 mm are observed to be geometrically similar (cf. figures 15(*a*), 15(*b*) and 15(*c*)). The separated shock angle is nearly a constant with a value of around 20.0° for the three impingement locations. This separation shock angle has a very good agreement with the theoretical value of around 19.4° using the LESF model. A comparison of the SWBLI between experimental and LESF model at $X_{ir} \approx 40$ mm is shown in figure 16.

It is noteworthy that the experimental and theoretical SWBLI are in close agreement with the exception of the flow at the reattachment location C. The shock waves, slip lines and expansion fan from the model are represented as continuous, dash-dotted and dotted lines, respectively, in figure 16. The separation bubble is the triangular region enclosed by the shear layer, the reattachment shear layer and the plate wall. The separated shock angle

X_{ir}	β_s	x'	L/X_{ir}	H/L	α
60 mm	19.6°	63.8 mm	1.05	0.131	0.726
50 mm	20.8°	50.6 mm	0.992	0.156	0.723
40 mm	19.0°	42.8 mm	1.07	0.146	0.705
Model, $\kappa = 1$	19.4°	$1.03X_{ir}$	1.03	0.159	0.811

Table 4. Comparison of separation bubble parameters between experiments and LESF model ($\kappa = 1$): separation shock angle β_s, reattachment location x', detachment length ratio L/X_{ir}, detachment bubble height ratio H/L and detachment bubble skewness α are used for comparison. For all cases, $M_\infty = 5.52$ and $\theta_w = 26.6°$.

relative to the free stream compares well with the experiment and model. The separated slip line in the model lies well within the growing shear layer in the experiments. The wedge shock–separation shock intersection, a Type I interaction, is slightly displaced by around 2 mm downstream of flow in the model because of a slightly larger wedge shock angle measured in the experiments $|\beta_w| \approx 38.5°$ when compared with $|\beta_w| \approx 36.9°$ using the θ_w-β_w-M_∞ oblique shock relation. Due to this small difference in β_w, the flow structures predicted by the model appear slightly elongated downstream of the flow. There is, however, a main difference in the reattachment shock clearly evident in figure 16 which is not captured by the model. The curving of the reattachment shock seen in experiments does not match with the normal reattachment shock angle in the model. The reason for this discrepancy is the curving of the reattachment shock due to the reattachment of the shear layer, which is not accounted for by the LESF model. In real flows, the shear layer reattachment causes the outer supersonic flow (immediately upstream of the reattachment and near the sonic line of the boundary layer) to be progressively ramped by a series of compression waves that focus into the reattachment shock. The interactions of the expansion fan (the expansion fan emanating from the reflection of the shock wave from the region of constant pressure, and the expansion fan emanating from the trailing edge of the wedge) also curve the reattachment shock downstream of the flow, but this is a secondary effect. The expansion fan effects emanating from the separation bubble apex (E1 in figure 7) and from the wedge trailing edge (peak pressure drop in figure 25*b*) may cause the curving of the reattachment shock in real flows. The turning of the reattaching shear layer from the plate wall is indeed a complex process in real flows which we do not account in the LESF model. Although the shock curvature can be only obtained from the experiments, the overall SWBLI pattern seems to resemble a near normal reattachment flow field. The separation length L measures at around 42.8 and 41.1 mm in the experiment and the LESF model respectively. The separation lengths are slightly larger compared with the inviscid shock impingement distance form the leading edge $L > X_{ir}$ (see figure 14*c*). The skewness α and the separation bubble height ratio H/L are also in good agreement between the experiments and the LESF model. We find that the near-sonic reattachment LESF model does not agree well with the flow field shown in figure 16. Table 4 shows the separation bubble characteristics between experiments and the LESF model.

For $X_{ir} \approx 40, 50$ and 60 mm the experiments show geometric similarity. First, we make a quick visual inspection of the structure of SWBLI in figures 15(*a*), 15(*b*) and 15(*c*) and find that they look geometrically similar. Note that the structures of the separated flows are said to be geometrically similar if they can be perfectly matched by simply enlarging or reducing the geometry. We also perform image processing to identify the shock coordinates and measure the angle of the separated shocks to obtain a

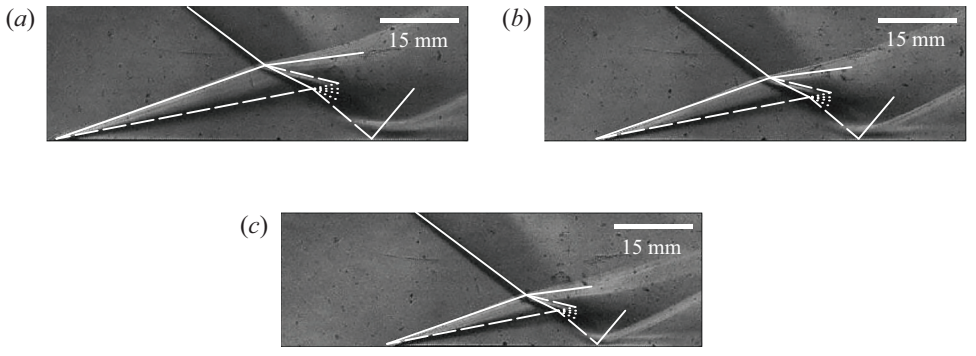

Figure 17. Separation bubble geometry between the experiments and the LESF model at shock impingement locations (*a*) $X_{ir} \approx 60$ mm, (*b*) $X_{ir} \approx 50$ mm and (*c*) $X_{ir} \approx 40$ mm. The figures clearly show a geometric similarity of the SWBLI at different shock impingements. The LESF model agrees well with the experiments. The shock wave, slip line and expansion fan of the LESF model are denoted by continuous, dashed and dotted lines, respectively. The model assumes $\kappa = 1$. For all cases in the figure, $M_\infty = 5.52$, $\theta_w = 26.6^\circ$.

quantitative comparison. The separated shock angles shown in table 4 are nearly the same for the different shock impingement locations, justifying the geometric similarity. Later, we show the wall pressure measurements which further justify the geometric similarity. Based on this evidence, we reason that there is a geometric similarity in the structure of SWBLI at $X_{ir} \approx 40$, 50 and 60 mm.

Figure 17 not only shows the geometric similarity for $X_{ir} \approx 40$, 50 and 60 mm, but also shows very good agreement with the LESF model. Note that the geometric similarity does not imply a fixed length scale, but a fixed geometry (i.e. fixed angles and length ratios).

4.3. *Transient flow*

Figure 18 shows the transient pressure readings on the plate wall at $X_{ir} \approx 40$ mm. Until around 2.4 ms the wall pressure sensors at 30, 38, 46, 54, 62 and 70 mm from the plate leading edge read noise having fluctuations of ± 0.3 kPa around zero mean value. The wall pressures slowly rise from around 2.4 ms and show a good correspondence to the Pitot pressure (cf. figure 4) which also begins to rise around the same time. The slow rise in the pressure sensors is followed by a steady time. The mean pressure steady times are different for each sensor location. For example, the 30 and 38 mm sensors in figure 18, which read the pressures inside the separation bubble (see figure 15 at $X_{ir} \approx 40$ mm for the separation bubble region), read mean pressure values of 11.2 and 26.4 kPa, respectively, between 3.2 and 3.6 ms. The sensor closest to the reattachment (reattachment location at 42.8 mm, see table 4), i.e. the 46 mm sensor picks up high fluctuations of ± 17 kPa and has a mean of around 69 kPa between 3.2 and 3.6 ms. A large amplitude pressure fluctuation is observed near the reattachment location since small movement of the reattachment shock causes significant variations in the wall pressures which are then picked up by the sensor. The wall pressures downstream of reattachment stabilize quickly and read lower pressures because of expansion fan interactions. The wall pressures downstream of reattachment are significantly lower, having values less than 60 kPa with mean pressure steady time between 3.0 and 3.6 ms.

The 600 µs Pitot steady time (between 3.0 and 3.6 ms) does not necessarily match with the 400 µs wall pressure steady time (between 3.2 and 3.6 ms) since separated flow, in general, require time for establishment. This establishment time was estimated to be

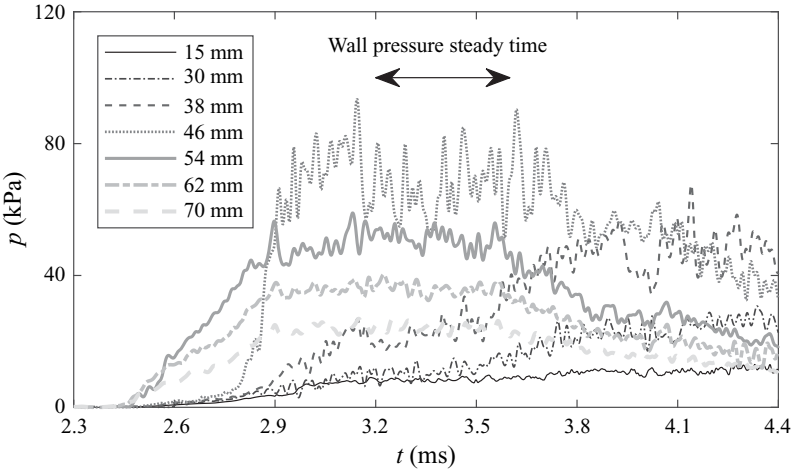

Figure 18. Time history of the wall pressure signals. The wall pressure steady times is between 3.2 and 3.6 ms. The 15 mm pressure sensor reads pressure inside the separation bubble and the 46 mm pressure sensor reads pressure near the reattachment location, which can both be verified by looking at the schlieren image in figure 15(*c*). For all cases in this figure, $\theta_w = 26.6^\circ$, $M_\infty = 5.52$ and $X_{ir} \approx 40$ mm.

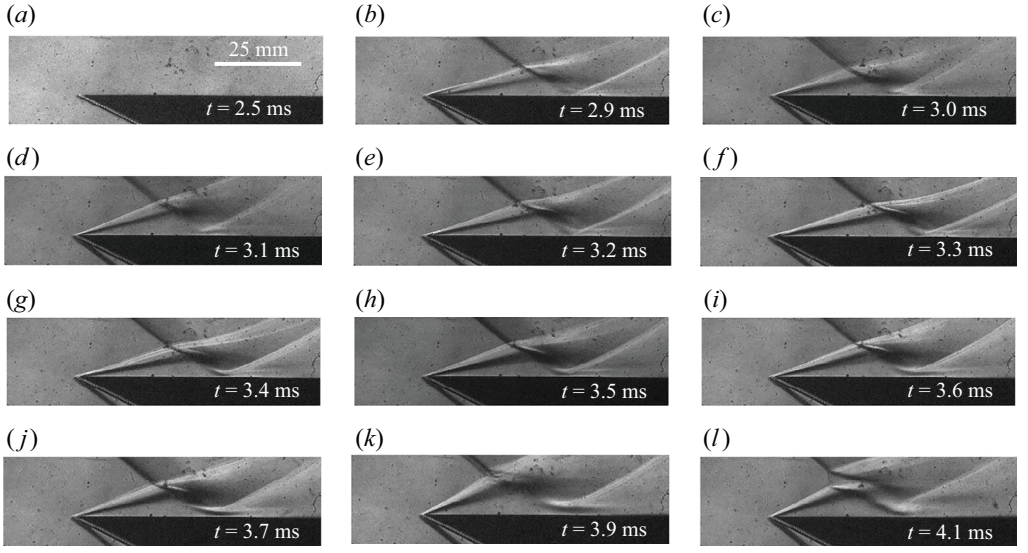

Figure 19. Schlieren time evolution of flow field for $X_{ir} \approx 40$ mm at $M_\infty = 5.52$ and $\theta_w = 26.6^\circ$.

around 200 µs by Sriram *et al.* (2016) for similar experimental conditions as in the present study. Thus, using this information, the wall pressure steady time is estimated around 400 µs from the available 600 µs Pitot steady time. The Pitot steady time and wall pressure steady time fit very well with the time evolution of flow in figure 19 explained later in this section.

The steady flow fields in figure 15 are taken from the schlieren time evolution of flow field during shock tunnel run time. The schlieren images have a temporal resolution of 50 µs. The steady flow structures in the schlieren images are visually checked within the duration of Pitot and wall pressure steady time. Figure 19 shows the time evolution of the

wedge shock–plate wall interaction for the $X_{ir} \approx 40$ mm impingement location. Both Pitot steady time (between 3.0 and 3.6 ms in figure 4) and wall pressures steady time (between 3.2 and 3.6 ms in figure 18) give a very good correspondence with the flow structures in the schlieren time evolution of the flow field. From three independent information types; Pitot signal, wall pressure signals and the schlieren time evolution images, the shock tunnel test time is estimated, which happens to be 400 µs between 3.2 and 3.6 ms in the present experiments.

4.4. *Wall pressure distribution*

To measure the wall pressures we make use of piezoelectric and Kulite pressure sensors. Kulite pressure sensors can be easily placed very close to the leading edge of the plate, since not very much material is required to support the sensors. They also have a better signal-to-noise ratio compared with PCB pressure sensors, but with the disadvantage of being very delicate and prone to damage.

A comparison of surface pressure distributions, for shock impingements of $X_{ir} \approx 60$, 50 and 40 mm, can also show whether the flow field is geometrically similar. Here, we note that it is difficult to accurately identify regions of constant pressure at each sensor location, e.g. in figure 18. This is mainly due to the pressure oscillations and the transient nature of the flow. However, the reported pressures are time average values after the separated shock seems to have reached the leading edge. The initial transient of the flow is nearly 200 µs between 3.0 and 3.2 ms and accounts for the establishment time of the separated flow, although the flow field is visibly steady throughout the Pitot steady time (Sriram *et al.* 2016).

Figure 20 shows the pressure distribution over the plate wall for three different impingement locations. The wall pressure distributions show some similarities compared with wall pressure distributions in a strong SWBLI (Délery & Marvin 1986), which is far from a shock reflection scenario (cf. figure 24*a*). The pressure distribution of a real (viscous) flow gives us information on two important quantities: plateau pressure and peak pressure. Plateau pressure, of the same order as separation pressure, is the static pressure inside the separation bubble region which is nearly constant within the bubble. Peak pressure, of the same order as reattachment pressure, is the highest pressure felt over the plate wall. It is to be noted here that the peak pressure, although being a local quantity, is approximated here as the peak pressure from among the signals sensed by the six pressure sensors.

Present experiments cannot precisely determine the reattachment pressures since no information on the location of zero wall shear stress is obtained. In the experiments, we report plateau pressures of approximately 7.82, 8.60 and 8.17 kPa for $X_{ir} \approx 60$, 50 and 40 mm, respectively.

To address the plateau pressures we performed some experiments using a Kulite sensor at 15 mm from the leading edge (we could place Kulites relatively close to the leading edge unlike the PCB sensors). The near leading-edge portion is always in the upstream portion of the bubble, and we observe the same pressure at 15 mm from the leading edge for all impingement locations, see figure 20. Due to the additional sensor in the upstream portion of the bubble, the averages of the pressure in the bubble are also closer for the different cases. This too suggests that the flow field is geometrically similar.

The difference in the average plateau pressure is due to the downstream most sensor in the bubble being closer to reattachment in a few cases, due to which they measure relatively higher pressure. The geometrical similarity is best noted in the sensors which

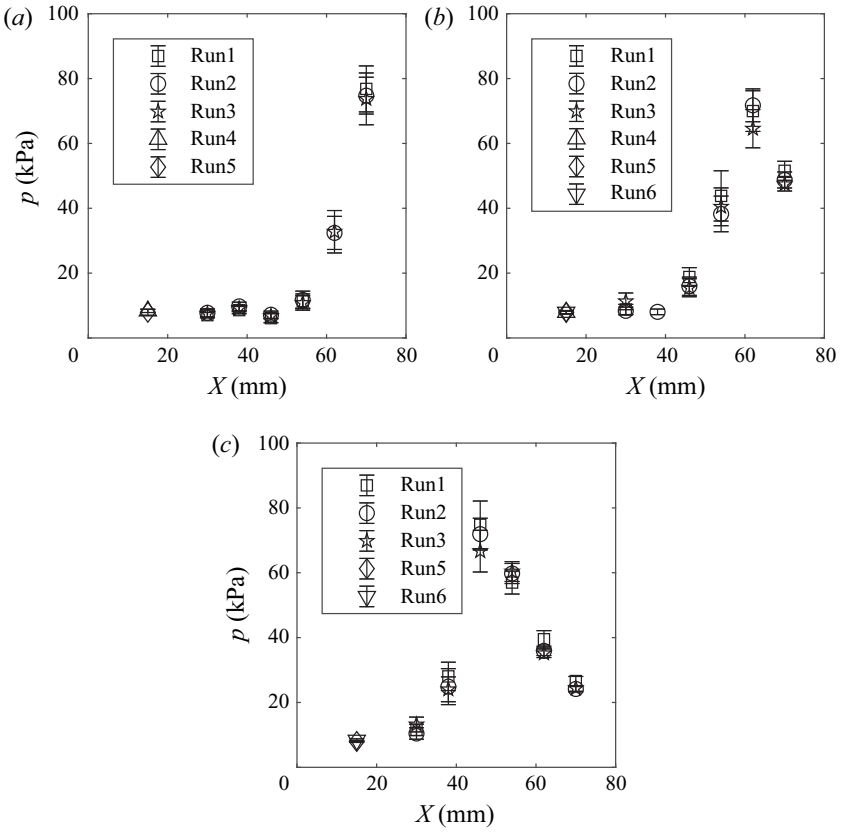

Figure 20. Pressure distribution on the plate wall. The pressure at each sensor location is averaged between 3.2 and 3.6 ms. The mean and error bar values of pressure are based on transient pressure data at each sensor location and at each run; (*a*) $X_{ir} \approx 60$ mm, (*b*) $X_{ir} \approx 50$ mm and (*c*) $X_{ir} \approx 40$ mm. For all cases in this figure, $M_\infty = 5.52$ and $\theta_w = 26.6^\circ$.

are in the most upstream location. At 15 mm from the leading edge, the same pressure of 8.0 kPa is observed for all impingement locations, illustrating the geometrical similarity.

The LESF model ($\kappa = 1$) for a similar experimental condition as in figure 20 gives the pressure inside the separation bubble as 7.67 kPa.

The plateau pressure is then followed by a gradual increase to the peak pressure which then subsequently decreases due to expansion fan interactions. This gradual increase and decrease in pressure near the reattachment location can also be seen in the transient pressure signals (cf. figure 18). For $X_{ir} \approx 50$ and 40 mm, the plateau pressure increases to peak pressures of around 69 and 71 kPa, respectively, which then subsequently decreases.

In the case where $X_{ir} \approx 60$ mm, the pressure sensor at 70 mm is located near the neck region (or near reattachment location) and reads an average value of 75 kPa, which is higher than that of sensors at other locations. The present experiments have a limitation in the spatial resolution of the surface pressure measurement, i.e. a minimum sensor-to-sensor distance of 8 mm. The closest sensor that can be placed downstream of 70 mm can only be 78 mm from the leading edge. We argue that a pressure measurement at 78 mm, sufficiently downstream of the neck region, would indicate a lower pressure than the sensor at 70 mm. An example of such lower pressure measurements downstream from the neck region can be seen in other shock impingements, e.g. at $X_{ir} \approx 40$ and 50

X_{ir}	Plateau pressure (avg.)	Sensors within separation bubble	Peak pressure (avg.)	Peak sensor location
60 mm	7.82 kPa	15, 30, 38, 46 mm	75.09 kPa	70 mm
50 mm	8.60 kPa	15, 30, 38 mm	68.76 kPa	62 mm
40 mm	8.17 kPa	15 mm	71.12 kPa	46 mm
Model, $\kappa = 1$	7.67 kPa $\approx 3.76 p_\infty$	—	118.52 kPa $\approx 58.1 p_\infty$	—

Table 5. Plateau pressure, peak pressure and sensor locations for $X_{ir} \approx [60, 50, 40]$ mm. Wall pressures in the inviscid model (normal reattachment) are compared with experiments at $M_\infty = 5.52$ and $\theta_w = 26.6^\circ$.

in figure 20. Therefore, we argue that, in the case of $X_{ir} \approx 60$ mm, the last pressure sensor, i.e. the 70 mm pressure sensor, would measure peak pressure compared with the 62 and 78 mm pressure sensors.

We therefore establish a geometrical similarity which can be seen from the shock angles (cf. table 4) and further illustrated from the measured the plateau pressures (cf. figure 20).

The average plateau and peak pressures along with the sensor locations are shown in table 5. A comparison with the LESF model ($\kappa = 1$) is also shown in table 5.

The measured peak pressure ratios in table 5 are around 1.65 times lower than the inviscid shock reflection pressure ratio. The possible reasons for the decrease in peak pressure are attributed to the inexact placement of the reattachment pressure sensors and the finite sensing area associated with the pressure sensor. Firstly, a small displacement in the location of the reattachment pressure sensor can cause a drop in the measurement of the peak pressure. Secondly, the pressure sensors have a finite area (diameter 5 mm) and hence average the pressure in a circular region. In any case, it is important to see that the measured peak pressures are of the same order as the inviscid shock reflection pressure ratio. For other impinging locations $X_{ir} \approx [30, 20, 10]$ mm, no transient pressure measurements are performed because the resulting small separated regions approach very close to the plate leading edge. We face the issue of mounting pressure sensors very close to the plate leading edge due to insufficient material required to hold the sensors.

4.5. *Validation of LESF model*

We have already validated the LESF model against experiments for the case of $M_\infty = 5.52$ and $\theta_w = 26.6^\circ$. The qualitative comparison is shown in figure 17. The quantitative comparisons are shown in tables 4 and 5. The LESF model is also verified for other wedge angles and free-stream conditions. We perform experiments at Mach 5.97 and 8.04 with a 21.80° wedge that depict a leading-edge separation flow. Note that the free-stream Mach number is varied by using different throat inserts. Figure 21 shows the experimental and LESF model flow field comparison. The LESF model with an oblique reattachment LESF model ($\kappa = 0$) for a 21.80° wedge shows a very good match with the experiments.

Although a normal reattachment solution exists for the flow conditions in figures 21(*a*) and 21(*b*), we find that it does not agree well with the experiments. We suppose the 21.80° wedge angle is an intermediate wedge angle which shows a near-sonic reattachment flow field (i.e. in the vicinity of the attached–detached transition). The comparison of the separated shock angle between experiments and LESF model is given in table 6.

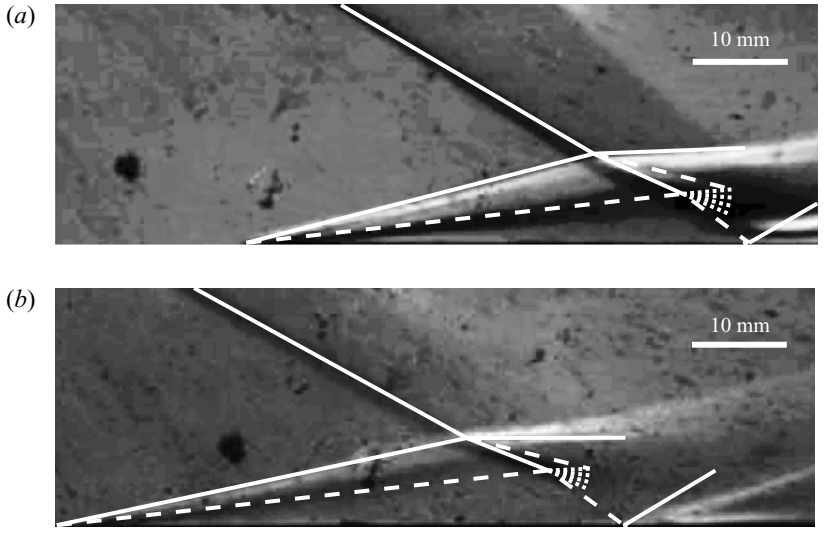

Figure 21. Comparison between the schlieren and LESF flow model using $\kappa = 0$ (*a*) $M_\infty = 5.97$, $\theta_w = 21.80^\circ$ and $X_{ir} \approx 50$ mm and (*b*) $M_\infty = 8.04$, $\theta_w = 21.80^\circ$ and $X_{ir} \approx 60$ mm.

Input		β_s comparison		Reference
M_∞	θ_w	Model	Experiments	
3	17°	31.2°, $\kappa = 0$	31.24°	Tao, Liu & Fan (2016)
5.52	26.6°	19.4°, $\kappa = 1$	20.0°	
5.97	21.8°	14.4°, $\kappa = 0$	13.5°	Present study
8.04	21.8°	12.0°, $\kappa = 0$	12.6°	

Table 6. Separation shock angle β_s comparison between present inviscid model and experiments depicting a leading-edge separation.

For a dual solution, we cannot precisely determine which combination of wedge angle and free-stream Mach number causes a normal or an oblique, the experiments can hint at the reattachment flow fields based on the overall structure of the SWBLI. While the experiments at Mach 5.54 and with a 26.6° wedge compare well with a LESF model having a normal reattachment, the experiments at Mach 5.97, 8.04 and with a 21.80° wedge compare well with an LESF model having an oblique reattachment. This does not come as a surprise since the 26.6° lies very close to $\theta_{w,max}$ whereas 21.80° lies very close to $\theta_{w,min}$ in figure 12(*b*). We suppose the near-sonic reattachments to occur at intermediate wedge angles around $\theta_w = \theta_{w,min}$ (cf. figure 12*b*) which is supported by our experiments.

We then compare the separated shock angle β_s obtained from the LESF model and from the experiments. The comparison is shown in table 6. For the LESF model, we solve for an oblique reattachment at $\theta_w = 17^\circ$, and a normal reattachment at $\theta_w = 26.6^\circ$. However, we solve for a oblique reattachment at $\theta_w = 21.8^\circ$. We suppose a near-sonic reattachment at intermediate wedge angle since there must be a transitional phase between the attached–detached reattachment. A good agreement in the separation shock angles gives confidence in the LESF model.

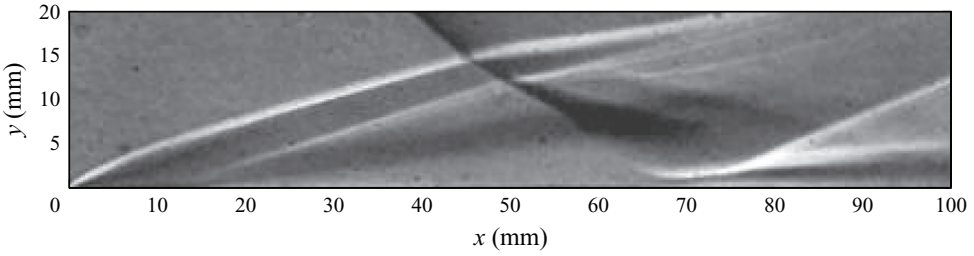

Figure 22. Flow separation at a downstream location from the leading edge. The separated flow field is shown for Mach 5.88 and 31° wedge at shock impingement location of 73 mm from the leading edge. Image taken from Sriram *et al.* (2016).

4.6. *Breaking geometric similarity*

We remark that the geometrically similar flow fields occur for a small range in Reynolds number. In our experiments with Mach 5.52 and a 26.6° wedge, the geometric similarity is only observed for shock impingement locations 40–60 mm from the leading edge or equivalently in the Reynolds number range 1.92×10^5–2.87×10^5. However, beyond this Reynolds number range we observe a breakage of geometric similarity for two situations: when shock impingement is either sufficiently far or sufficiently close to the leading edge. The terms sufficiently far and sufficiently close are used here since a precise impingement location causing the transition to geometric similarity breakage is not obtained in the present experiments.

For shock impingement sufficiently far away from the plate leading edge, flow separation occurs at some downstream location from the leading edge. For example, in figure 22 it is evident that the flow separation occurs at some downstream location. The shock impingement (inducing separation) causes the separation location to move upstream of (inviscid) impingement until mass flow balance of the separation bubble is reached; mass entering the bubble due to pressure rise at reattachment is balanced by mass leaving the bubble through mixing (shear) layers. While the overall geometry of the separated flow field is governed by the impinging shock strength, the flow in the onset of separation is governed by the free-interaction theory (Chapman *et al.* 1958).

Another breakage of geometric similarity occurs when shock impingement is sufficiently close to the plate leading edge. For example, in the present experiments, for $X_{ir} < 40$ mm from the plate leading edge (see figures 15(*d*), 15(*e*) and 15(*f*)) the breakage of geometric similarity occurs. An increase in the separation shock angle and a Type II wedge shock–separation shock interaction is the characteristic associated with the breakage of the geometric similarity. The reason for this breakage is not clear, although experiments by Mahapatra & Jagadeesh (2009) hint at inlet unstart phenomena in impulse facilities. It was observed that, as the cowl plate length decreased (similar effect to the shock impingement moving close to the plate leading edge), a transition from Type I to Type II shock–shock interaction was observed. The present LESF model does not account for a Type-II wedge shock–separation shock interaction and hence cannot explain the separation bubble geometries for Type-II interactions.

5. Conclusion

In this work, we perform theoretical modelling and experiments of leading-edge separation over a plate wall caused by means of an impinging shock. The considered impinging shock

strengths are an order of magnitude larger than the incipient pressures required to cause flow separation. The resultant separation bubbles are 'large' (Sriram & Jagadeesh 2014) and scale directly with the distance of shock impingement from the plate leading edge. The theoretical model is iteratively solved for a system of shocks, expansion fan and slip lines. The experiments use schlieren visualizations and surface pressure measurements in order to characterize the separation flow fields.

We first construct a LESF model which derives from the separated flow model proposed by Délery & Marvin (1986). The model describes a 2-D steady state inviscid flow field over a plate wall. The LESF model is bifurcated based on two reattachment flow fields: an oblique reattachment and a normal reattachment. Critical wedge angles 16°–19° are identified for free-stream Mach numbers 5–8, where neither an oblique nor a normal reattachment occurs. We speculate a near-sonic reattachment at around the critical wedge angle which bridges the gap between the two reattachments. Contrary to expectations, the LESF model predicts large scale and roughly symmetric separation bubbles for an oblique reattachment when compared with a normal reattachment. This is due to strong separation shocks as compared with the reattachment shocks in oblique reattachment situations. However, in normal reattachment situations the reattachment shocks are much stronger than the separation shocks which give rise to small scale and skewed separation bubbles. Through the LESF model, we provide rationale for two important questions: (a) why is a normal reattachment preferred for strong impinging shocks? and (b) why does the separation length, for strong impinging shocks, scale directly with the distance of shock impingement from the plate leading edge?

Next, we perform experiments of a wedge shock impinging near a plate wall leading edge. The wedge shock is generated by a 26.6° wedge in a Mach 5.52 flow. For a small range of shock impingement locations, the separations occur at the plate leading edge and are geometrically similar. The self-similarity is confirmed by the geometrical structure of the SWBLI, the pressures inside the separation bubble and the peak pressure over the plate wall remain nearly constant. The size of the separation bubble, separation bubble pressure, Type I wedge shock–separation shock interaction and other separated flow features predicted by the LESF model have a very good agreement with the experiments. Although, the model fails to predict curvature of the reattachment shock near the reattachment location, the overall flow structure nevertheless resembles a near normal reattachment as compared with an oblique reattachment. At intermediate wedge angles of 21.80°, the flow fields have a good agreement with an oblique reattachment. The geometric self-similarity breaks when shock impingements occur sufficiently close to or sufficiently far away from the plate leading edge, which has been reported in the literature. The reasons for this are attributed to the inlet unstart phenomena in impulse facilities and the free-interaction phenomenon, respectively, which influences the separated flow field.

The prediction of separated flow fields in a hypersonic free stream has proven challenging owing to the complex interaction patterns formed between the impinging shocks and boundary layers. However, when a strong shock impingement causes leading-edge separation, typical in scramjet engine inlets, the resultant separated flow field can be modelled as inviscid and therefore the separation bubble characteristics can be well anticipated. The separated flow field happens to be viscosity independent since the complicated development of the boundary layer and its associated pressure variations from plate leading edge to separation location are completely avoided (Chapman *et al.* 1958). We find that the separated flow fields predicted by the LESF model

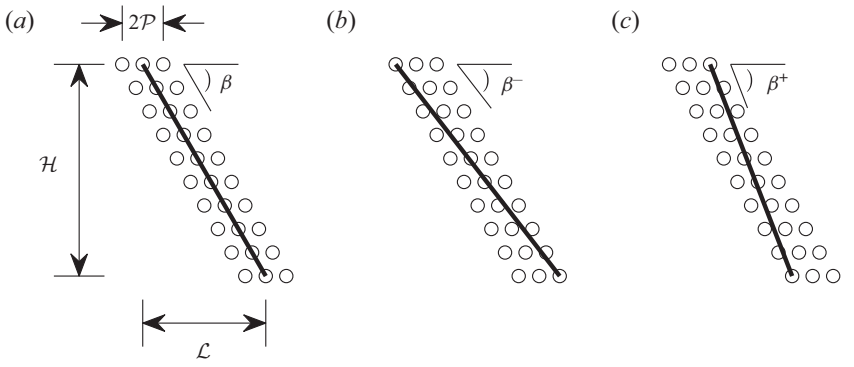

Figure 23. Schematic diagram of a shock wave that is detected in the experiments. The shock wave coordinates are captured by either choosing local bright or dark pixels. The uncertainty in the shock wave location in the x-coordinate is $\pm\mathcal{P}$.

has a very good agreement with the experiments which gives reasonable confidence in the assumptions
used.

Acknowledgements. The authors would like to thank Professor N. Balakrishnan, Department of Aerospace Engineering, IISc for providing access to use HiFUN CFD tool. We thank A. Bajpayee for performing the experiments with the Kulite sensors. The authors are grateful to Defense Research and Development Organization, India, for their financial support to the research activities in the Laboratory for Hypersonic and Shock wave Research, Indian Institute of Science, Bengaluru.

Declaration of interests. The authors report no conflict of interest.

Author ORCIDs.
L. Srinath https://orcid.org/0000-0002-0563-7022;
R. Sriram https://orcid.org/0000-0001-7874-565X;
G. Jagadeesh https://orcid.org/0000-0002-5495-9351.

Appendix A. Validation of M_∞ and P_∞ in HST2

The free-stream Mach number M_∞ in the experiments can be verified by the θ_w-β_w-M_∞ oblique shock relation (Anderson 1990)

$$\tan\theta_w = 2\cot\beta_w\left[\frac{M_\infty^2\sin^2\beta_w - 1}{M_\infty^2\,(\gamma + \cos 2\beta_w) + 2}\right]. \tag{A1}$$

Assuming that $\theta_w = 26.6^\circ$ and $M_\infty = 5.52$, we get $\beta_w = 36.9^\circ$ from (A1). Now we check the wedge shock angle β_w in the experiments noted for two scenarios: different experiments (e.g. at each shock location in figure 15) and within the time duration of each experiment (e.g. during stationary time in figure 19). Both scenarios yield an average $\beta_w = 38.1^\circ$ with a mean absolute deviation of 0.67°. Furthermore, the uncertainty in β_w may come from the image processing.Figure 23 shows a schematic diagram of a shock wave that is detected by an intensity scan in the images. The intensity scan can detect a local region of bright/dark pixels in the image, shown as circles in the figure, associated with the coordinates of a shock. The uncertainty in the measurement of the shock wave angle $\Delta\beta$ is due to the uncertainty in the x-pixel position $\mathcal{P}$, the vertical length scale of

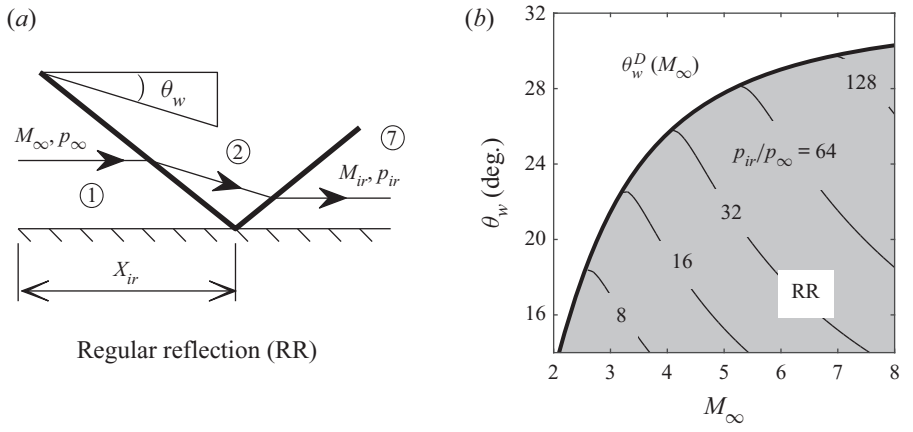

Figure 24. Theoretical modelling of a shock reflection problem: (*a*) Schematic drawing of a RR. Regions 1 and 7 denote the conditions in the free stream and post-reattachment, respectively. The shock impingement location from the leading edge of the plate wall is X_{ir}. (*b*) The phase diagram θ_w vs M_∞ for an air flow ($\gamma = 1.40$). The domain of RR is shown in the grey shaded region superimposed by p_{ir}/p_∞ contour lines.

the shock wave $\mathcal{H}$ and the shock angle itself β. It can be easily shown that for $2\mathcal{P} \ll \mathcal{L}$, $\Delta\beta$ is given by

$$\Delta\beta = \tan^{-1}\left(\frac{2\mathcal{P}}{\mathcal{H}}\sin^2\beta\right). \tag{A2}$$

Here, $\Delta\beta = \beta^+ - \beta = \beta - \beta^-$. In the experiments, we have the following parameters for the wedge shock: $\mathcal{P} = 2$ pixels, $\mathcal{H} = 130$ pixels and $\beta_w = 38.1^\circ$, resulting in $\Delta\beta_w \approx 0.67^\circ$. We note that the difference in β_w between the experiment and the theory (i.e. $2\Delta\beta$) is well within the overall uncertainty of the present experiments. Equation (A2) is applicable to separation shock angles as well.

The free-stream static pressure p_∞ can be verified by the shock jump expression (Anderson 1990)

$$\frac{p_2}{p_\infty} = \frac{2\gamma M_\infty^2 \sin^2\beta_s - (\gamma - 1)}{(\gamma + 1)}. \tag{A3}$$

Assuming that $M_\infty = 5.52$, $\beta_s = 20^\circ$, and $p_\infty = 2.04$ kPa, we get $p_2 \approx 8.14$ kPa. Note that we take an average value of β_s from table 4. Since p_2 corresponds to the dead air inside the separation bubble, we compare the two values, i.e. p_2 from the theory and p_d from the experiments; p_d remains nearly constant (cf. Figure 20 and table 5) and has an average value of $p_d \approx 8.20$ kPa with an uncertainty of less than 1 kPa. Similar to the wedge angle, the difference in separation bubble pressure (p_2 or p_d) between experiment and theory is also well within the uncertainty of the present experiments.

Within the uncertainties of the measured wedge shock angle and the measured pressures inside the separation bubble, we validate the free-stream parameters namely the Mach number and static pressure. The free-stream parameters in HST2 were previously verified by measuring the shock stand-off distance for spherical models (Thakur & Jagadeesh 2017) and the stagnation point heat transfer of a blunt cone model (Srinath & Reddy 2015). Nevertheless, we note that the estimation of the free stream by the Pitot measurement is better and more accurate compared with other measurements for a shock tunnel.

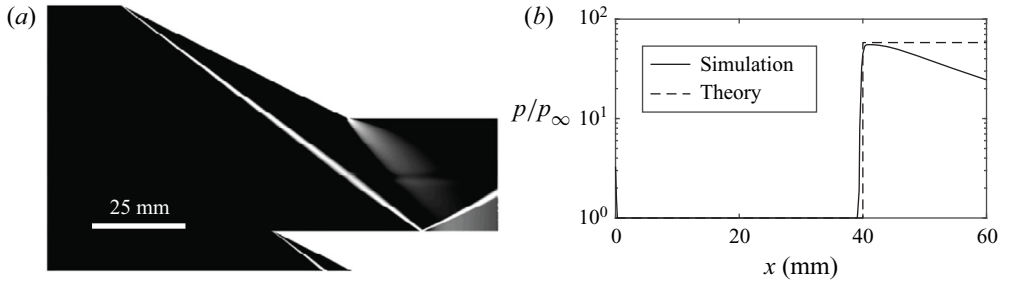

Figure 25. Simulation results of a shock reflection problem: (*a*) 2-D contour of the static pressure gradient and (*b*) pressure distribution at the plate wall. The peak pressure ratio at the plate wall $p_{ir}/p_\infty \approx 55$ agrees well between the simulation and the theory. For all cases in the figure, $\theta_w = 26.6^\circ$, $M_\infty = 5.52$ and $X_{ir} \approx 40$ mm.

Appendix B. Estimation of θ_w^D and p_{ir}/p_∞

In principle, the scenario of a regular reflection (RR) from a plate wall in a perfect gas has been completely solved by Von Neumann (1943). However, we give here the theoretical estimates of two important quantities: θ_w^D and p_{ir}/p_∞, as a reference.

Figure 24(*a*) shows the schematic of RR, which consists of a configuration with two shocks: a wedge shock and a reflected shock. The wedge shock impinges at the location X_{ir} from the leading edge of the flat plate. Also shown is a streamline that is parallel to the free-stream flow in region 1, which is deflected toward the plate wall by the wedge shock in region 2, and once again made parallel to the free-stream flow by the reflected shock in region 7. Note that region 1 denotes the free-stream conditions, i.e. $M_1 = M_\infty$ and $p_1 = p_\infty$, and that region 7 denotes the post-reattachment conditions, i.e. $M_7 = M_{ir}$ and $p_7 = p_{ir}$, where the subscript '*ir*' denotes the inviscid (shock) reflection. Figure 24(*b*) shows the θ_w vs M_∞ phase diagram, representing the domain (grey shaded area) where RR can possibly occur. For a fixed M_∞, RR can occur when $\theta_w < \theta_w^D(M_\infty)$. For $\theta_w > \theta_w^D(M_\infty)$ an irregular reflection occurs, the details of which can be found in the work of Ben-Dor (2007). Here, θ_w^D is denoted as the detached wedge angle that occurs when $M_{ir} = 1$. We note that, for a fixed γ, θ_w^D is only a function of M_∞ and p_{ir}/p_∞ is only a function of M_∞ and θ_w, which are computed numerically since they have no closed-form solutions. For an air flow ($\gamma = 1.40$), the estimates for θ_w^D and p_{ir}/p_∞ are also given in the figure.

The experiments in the present study mainly use $\theta_w = 26.6^\circ$ and $M_\infty = 5.52$, for which $p_{ir}/p_\infty \approx 55$, from the theory. We perform a numerical simulation to check whether this pressure ratio is affected by the expansion fan from the convex corner of the wedge. The simulation assumes a 2-D steady state Euler flow, performed in collaboration with the Center of Excellence in Hypersonics, IISc Bengaluru, using the in-house finite volume code High Resolution Flow Solver on Unstructured meshes (HiFUN) (Shende & Balakrishnan 2004). The simulation uses the free-stream conditions from table 1, the experimental model set-up as shown in figure 6 and the shock impingement location $X_{ir} \approx$ 40 mm. The 2-D pressure gradient contour from the simulation is shown in figure 25(*a*). The comparison of the wall pressure between the simulation and the theory is shown in figure 25(*b*). We note that the peak pressure ratio at the plate wall agrees very well with the theory, indicating that the expansion fan does not affect the pressure ratio immediately downstream of the reflected shock. We remark that the pressure ratio imposed on the plate wall, i.e. p_{ir}/p_∞, is a characteristic quantity related to the wedge θ_w and the Mach number of the free stream M_∞, and plays an important role in the LESF model.

Appendix C. Separation bubble characteristics for $\kappa = 0$ and $\kappa = 1$

Mach number	Wedge angle	Separation bubble characteristics						Reattachment pressure ratio
M_∞	θ_w	β_s	$\frac{p_d}{p_\infty}$	$\frac{p_d}{p'}$	$\frac{L}{X_{ir}}$	$\frac{H}{L}$	α	$\frac{p'}{p_\infty} = \frac{p_{ir}}{p_\infty}$
			Oblique reattachment $\kappa = 0$					
5	9°	23.9°	4.63	0.72	3.01	0.054	0.205	6.47
	12°	26.8°	5.74	0.56	2.03	0.093	0.299	10.4
	15°	29.9°	7.06	0.46	1.70	0.128	0.352	15.5
6	9°	22.4°	5.92	0.68	2.80	0.055	0.209	8.70
	12°	25.5°	7.60	0.52	1.94	0.094	0.297	14.6
	15°	28.9°	9.62	0.43	1.64	0.130	0.346	22.4
7	9°	21.2°	7.29	0.64	2.52	0.058	0.223	11.5
	12°	24.5°	9.68	0.49	1.83	0.096	0.303	19.9
	15°	28.2°	12.6	0.40	1.58	0.132	0.348	31.1
8	9°	20.2°	8.75	0.59	2.29	0.062	0.239	14.8
	12°	23.8°	12.0	0.46	1.74	0.099	0.311	26.3
	15°	27.6°	15.9	0.38	1.52	0.134	0.352	41.7
			Normal reattachment $\kappa = 1$					
5	20°	12.7°	1.24	0.046	1.00	0.030	0.963	26.7
	23°	15.8°	1.99	0.057	1.01	0.092	0.890	35.1
	26°	20.0°	3.26	0.072	1.03	0.154	0.815	45.2
6	20°	11.2°	1.41	0.036	0.998	0.040	0.949	39.5
	23°	13.9°	2.26	0.044	1.00	0.092	0.889	51.8
	26°	17.3°	3.56	0.054	1.02	0.143	0.832	65.9
7	20°	10.2°	1.62	0.029	0.995	0.047	0.938	55.4
	23°	12.7°	2.58	0.035	0.998	0.093	0.885	72.6
	26°	15.7°	4.02	0.044	1.01	0.137	0.838	91.7
8	20°	9.44°	1.84	0.025	0.992	0.053	0.929	74.5
	23°	11.8°	2.93	0.030	0.995	0.094	0.883	97.4
	26°	14.6°	4.55	0.037	1.01	0.134	0.841	122

Appendix D. Effect of finite span

We briefly study the structure of SWBLI in the experiments at two different spans: 100 and 120 mm. Note that the span is changed jointly for both the wedge and the flat plate. The reason for choosing these two spans is that the models would be well within the core flow diameter of the shock tunnel. It is worthwhile studying the finite effects of the span, because it tells us whether the flow is three-dimensional.

Figure 26 shows the schlieren images of steady SWBLIs for two different spans. The experiments were performed at similar free-stream Mach numbers and wedge angles, given in table 1. However, the location of the inviscid shock impingement location is slightly different for the two spans, so it is useful to compare only the geometric aspects of the separated bubble and not its absolute length scales.

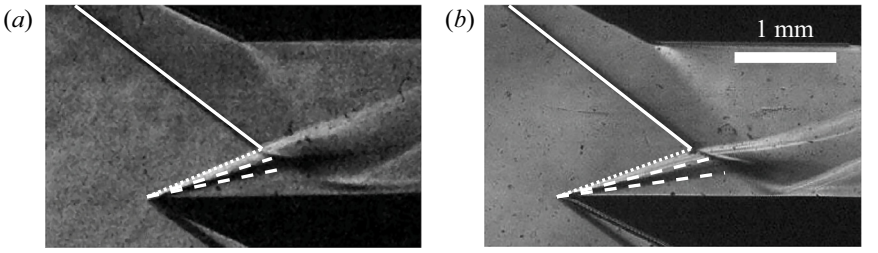

Figure 26. LESF fields at two different spans: (*a*) 100 mm and (*b*) 120 mm. The shock impingement locations are $X_{ir} \approx 35$ and 40 mm for the spans 100 and 120 mm, respectively. The solid, dotted and dashed lines represent the wedge shock, the separation shock and the extents of the shear layer, respectively, obtained from image processing. For all cases in the figure, $M_\infty = 5.52$ and $\theta_w = 26.6^\circ$.

We compare two important parameters: wedge shock angle and separated shock angle. The wedge angle for the 100 mm span is 0.7° smaller than that of the 120 mm span. The separation shock angle for the 100 mm span is 2.0° larger than that of the 120 mm span. Note that the overall uncertainty is 1.6° and 2.2° for the wedge shock angle and the separated shock angle, respectively. Although the shock angles are slightly different for the two spans, they are well within the measurement uncertainty of the shock angles in the experiments.

References

Anderson, J.D. 1990 *Modern Compressible Flow: With Historical Perspective*, vol. 12. McGraw-Hill.

Babinsky, H. & Harvey, J.K. 2011 *Shock Wave-Boundary-Layer Interactions*, vol. 32. Cambridge University Press.

Ben-Dor, G. 2007 *Shock Wave Reflection Phenomena*, vol. 2. Springer.

Bogdonoff, S.M. & Kepler, C.E. 1955 Separation of a supersonic turbulent boundary layer. *AIAA J.* **22** (6), 414–430.

Borovoy, V.Y., Egorov, I.V., Skuratov, A.S. & Struminskaya, I.V. 2013 Two-dimensional shock-wave/boundary-layer interaction in the presence of entropy layer. *AIAA J.* **51** (1), 80–93.

Brower, W.B. Jr. 1961 Leading-edge separation of laminar boundary layers in supersonic flow. *AIAA J.* **28** (12), 957–961.

Burggraf, O.R. 1975 Asymptotic theory of separation and reattachment of a laminar boundary layer on a compression ramp. In *Proc. AGARD Symp. on Flow Separation, Göttingen*. AGARD-CP-168.

Chapman, D.R. 1950 Laminar mixing of a compressible fluid. NACA Tech. Rep. TR-958.

Chapman, D.R. 1956 A theoretical analysis of heat transfer in regions of separated flow. NACA Tech. Rep. TN-3792.

Chapman, D.R., Kuehn, D.M. & Larson, H.K. 1958 Investigation of separated flows in supersonic and subsonic streams with emphasis on the effect of transition. NACA Tech. Rep. 1356.

Clemens, N.T. & Narayanaswamy, V. 2014 Low-frequency unsteadiness of shock wave/turbulent boundary layer interactions. *Annu. Rev. Fluid Mech.* **46**, 469–492.

Davis, J.P. & Sturtevant, B. 2000 Separation length in high-enthalpy shock/boundary-layer interaction. *Phys. Fluids* **12** (10), 2661–2687.

Délery, J. & Dussauge, J.P. 2009 Some physical aspects of shock wave/boundary layer interactions. *Shock Waves* **19** (6), 453.

Délery, J. & Marvin, J.G. 1986 Shock-wave boundary layer interactions. NATO Tech. Rep. AGARD-AG-280.

Dolling, D.S. 2001 Fifty years of shock-wave/boundary-layer interaction research: what next? *AIAA J* **39** (8), 1517–1531.

Edney, B.E. 1968 Effects of shock impingement on the heat transfer around blunt bodies. *AIAA J.* **6** (1), 15–21.

Elfstrom, G.M. 1972 Turbulent hypersonic flow at a wedge-compression corner. *J. Fluid Mech.* **53** (1), 113–127.

GADD, G.E. 1957 A theoretical investigation of laminar separation in supersonic flow. *J. Aeronaut. Sci.* **24** (10), 759–771.

GADD, G.E., HOLDER, D.W. & REGAN, J.D. 1954 An experimental investigation of the interaction between shock waves and boundary layers. *Proc. R. Soc. Lond.* A **226** (1165), 227–253.

GAITONDE, D.V. 2015 Progress in shock wave/boundary layer interactions. *Prog. Aerosp. Sci.* **72**, 80–99.

GANAPATHISUBRAMANI, B., CLEMENS, N.T. & DOLLING, D.S. 2007 Effects of upstream boundary layer on the unsteadiness of shock-induced separation. *J. Fluid Mech.* **585**, 369–394.

GREEN, J.E. 1970 Interactions between shock waves and turbulent boundary layers. *Prog. Aerosp. Sci.* **11**, 235–340.

HAKKINEN, R.J., GREBER, I., TRILLING, L. & ABARBANEL, S.S. 1959 The interaction of an oblique shock wave with a laminar boundary layer. NASA Memo 2-18-59W.

HAYAKAWA, K. & SQUIRE, L.C. 1982 The effect of the upstream boundary-layer state on the shock interaction at a compression corner. *J. Fluid Mech.* **122**, 369–394.

HAYES, W.D. & PROBSTEIN, R.F. 1959 *Hypersonic Flow Theory*. Academic Press.

KATZER, E. 1989 On the lengthscales of laminar shock/boundary-layer interaction. *J. Fluid Mech.* **206**, 477–496.

KHRAIBUT, A., GAI, S.L., BROWN, L.M. & NEELY, A.J. 2017 Laminar hypersonic leading edge separation-a numerical study. *J. Fluid Mech.* **821**, 624.

KREK, R.M. & JACOBS, P.A. 1993 STN, shock tube and nozzle calculations for equilibrium air. *Tech. Rep.* Research Report No. 2/93, The University of Queensland.

KULKARNI, V. 2007 Investigation of flow modification techniques to reduce drag and heat transfer for large angle blunt cones in high enthalpy flows. PhD thesis, Indian Institute of Science.

LEES, L. & REEVES, B.L. 1964 Supersonic separated and reattaching laminar flows. I. General theory and application to adiabatic boundary-layershock-wave interactions. *AIAA J.* **2** (11), 1907–1920.

LIEPMANN, H.W., ROSHKO, A. & DHAWAN, S. 1951 On reflection of shock waves from boundary layers. NACA Tech. Note YN-2334.

LOTH, E. & MATTHYS, M.W. 1995 Unsteady low Reynolds number shock boundary layer interactions. *Phys. Fluids* **7** (5), 1142–1150.

MAHAPATRA, D. 2010 Investigation of ramp/cowl shock interaction processes near a generic scramjet inlet at hypersonic mach number. PhD thesis, Indian Institute of Science.

MAHAPATRA, D. & JAGADEESH, G. 2009 Studies on unsteady shock interactions near a generic scramjet inlet. *AIAA J.* **47** (9), 2223–2232.

MALLINSON, S.G., GAI, S.L. & MUDFORD, N.R. 1997 The interaction of a shock wave with a laminar boundary layer at a compression corner in high-enthalpy flows including real gas effects. *J. Fluid Mech.* **342**, 1–35.

MATHEIS, J. & HICKEL, S. 2015 On the transition between regular and irregular shock patterns of shock-wave/boundary-layer interactions. *J. Fluid Mech.* **776**, 200–234.

MOFFAT, R.J. 1988 Describing the uncertainties in experimental results. *Exp. Therm Fluid Sci.* **1** (1), 3–17.

NEEDHAM, D. & STOLLERY, J. 1966 Boundary layer separation in hypersonic flow. In *3rd and 4th Aerospace Sciences Meeting. AIAA Paper* 1966-0455.

PRAKASH, R., LE PAGE, L.M., MCQUELLIN, L.P., GAI, S.L. & O'BYRNE, S. 2019 Direct simulation monte carlo computations and experiments on leading-edge separation in rarefied hypersonic flow. *J. Fluid Mech.* **879**, 633–681.

SETTLES, G.S. 2001 *Schlieren and Shadowgraph Techniques-Visualizing Phenomena in Transparent Media*. Springer.

SHARP, A.W. 1959 The supersonic flow past a leading edge separation bubble. *J. Fluid Mech.* **5** (3), 445–459.

SHENDE, N. & BALAKRISHNAN, N. 2004 HIFUN-3D-1 users manual. *Tech. Rep.* Dept. of Aerospace Engineering, Fluid Mechanics Rept. 2004 FM 10.

SRINATH, L. 2015 Experimental investigations of leading edge bluntness in shock boundary layer interactions at hypersonic speeds. Master's thesis, Indian Institute of Science.

SRINATH, L., SRIRAM, R. & JAGADEESH, G. 2017 Shock-induced large separation bubbles near the leading edge of a flat plate at hypersonic mach numbers. In *30th International Symposium on Shock Waves 2* (ed. G. Ben-Dor, O. Sadot & O. Igra), pp. 1189–1193. Springer.

SRINATH, S. & REDDY, K.P.J. 2015 Large carbon cluster thin film gauges for measuring aerodynamic heat transfer rates in hypersonic shock tunnels. *Meas. Sci. Technol.* **26** (2), 025901.

SRIRAM, R. 2013 Shock tunnel investigations on hypersonic impinging boundary layer interaction. PhD thesis, Indian Institute of Science.

SRIRAM, R. & JAGADEESH, G. 2014 Shock tunnel experiments on control of shock induced large separation bubble using boundary layer bleed. *Aerosp. Sci. Technol.* **36**, 87–93.

SRIRAM, R. & JAGADEESH, G. 2015 Correlation for length of impinging shock-induced large separation bubble at hypersonic speed. *AIAA J.* **53** (9), 2771–2776.

SRIRAM, R., SRINATH, L., DEVARAJ, M.K.K. & JAGADEESH, G. 2016 On the length scales of hypersonic shock-induced large separation bubbles near leading edges. *J. Fluid Mech.* **806**, 304–355.

STEWARTSON, K. & WILLIAMS, P.G. 1969 Self-induced separation. *Proc. R. Soc.* A **312** (1509), 181–206.

STOLLERY, J.L. & BATES, L. 1974 Turbulent hypersonic viscous interaction. *J. Fluid Mech.* **63** (1), 145–156.

TAO, Y., LIU, W.D. & FAN, X.Q. 2016 Investigation of shock-induced boundary layer separation extended to the flat plate leading-edge. *Acta Mechanica* **227** (6), 1791–1797.

THAKUR, R. & JAGADEESH, G. 2017 Experimental analysis of shock stand-off distance over spherical bodies in high-enthalpy flows. *Proc. Inst. Mech. Engrs* G **231** (14), 2666–2676.

VERMA, S.B. & CHIDAMBARANATHAN, M. 2015 Transition control of Mach to regular reflection induced interaction using an array of micro ramp vane-type vortex generators. *Phys. Fluids* **27** (10), 107102.

VON NEUMANN, J. 1943 Oblique reflection of shocks. *Tech. Rep.* 12. Bur. Ord. Explosives Research Rept.

WAGNER, J.L., YUCEIL, K.B., VALDIVIA, A., CLEMENS, N.T. & DOLLING, D.S. 2009 Experimental investigation of unstart in an inlet/isolator model in Mach 5 flow. *AIAA J.* **47** (6), 1528–1542.

WU, M. & MARTIN, M.P. 2008 Analysis of shock motion in shockwave and turbulent boundary layer interaction using direct numerical simulation data. *J. Fluid Mech.* **594**, 71–83.